

## L AND T DWARF MODELS AND THE L TO T TRANSITION

ADAM BURROWS<sup>1</sup>, DAVID SUDARSKY<sup>1</sup>, & IVAN HUBENY<sup>1</sup>

*Accepted to the Ap. J.*

### ABSTRACT

Using a model for refractory clouds, a novel algorithm for handling them, and the latest gas-phase molecular opacities, we have produced a new series of L and T dwarf spectral and atmosphere models as a function of gravity and metallicity, spanning the  $T_{\text{eff}}$  range from 2200 K to 700 K. The correspondence with observed spectra and infrared colors for early- and mid-L dwarfs and for mid- to late-T dwarfs is good. We find that the width in infrared color-magnitude diagrams of both the T and L dwarf branches is naturally explained by reasonable variations in gravity and, therefore, that gravity may be the “second parameter” of the L/T dwarf sequence. We investigate the dependence of theoretical dwarf spectra and color-magnitude diagrams upon various cloud properties, such as particle size and cloud spatial distribution. In the region of the L→T transition, we find that no one cloud-particle-size and gravity combination can be made to fit all the observed data, though the role of binarity in the extant L and T dwarf data sets has yet to be fully determined. However, our results suggest that current ignorance of detailed cloud meteorology renders ambiguous the extraction of various physical quantities such as  $T_{\text{eff}}$  and gravity for mid-L to early-T dwarfs. Nevertheless, for decreasing  $T_{\text{eff}}$ , we capture with some accuracy the transition from CO to CH<sub>4</sub> in the *K* band, the FeH and CrH features at  $\sim 1.0 \mu\text{m}$  and  $\sim 0.85 \mu\text{m}$  (at least for the early- to mid-Ls), the emergence of the neutral Na, K, Cs, and Rb alkali features, the growth of the *Y/Z* band peak, the disappearance of TiO and VO in L dwarfs, the evolution in the shapes of the *J*, *H*, and *K* bands, and the evolution of the K I features near  $1.25 \mu\text{m}$  and  $1.17 \mu\text{m}$ . We speculate that the subdwarf branch of the L dwarfs will be narrower in effective temperature, and, that for low enough metallicity, the L dwarfs will disappear altogether as a spectroscopic class. Furthermore, we note that the new, lower solar oxygen abundances of Allende-Prieto, Lambert, & Asplund (2002) produce better fits to brown dwarf data than do the older values. Finally, we discuss various issues in cloud physics and modeling and speculate on how a better correspondence between theory and observation in the problematic L→T transition region might be achieved.

*Subject headings:* general—stars: low-mass, brown dwarfs—radiative transfer—molecular processes—  
infrared: stars

### 1. INTRODUCTION

In the last ten years since the first identification of T and L dwarfs in the solar neighborhood, more than sixty T dwarfs and hundreds of L dwarfs have been classified spectroscopically and photometrically (Oppenheimer et al. 1995; Delfosse et al. 1997; Burgasser et al. 1999,2000a,b,c; Kirkpatrick et al. 1999,2000; Geballe et al. 2002; Martín et al. 1999; Cruz et al. 2003; Knapp et al. 2004; Golimowski et al. 2004). Both infrared and optical spectral features and colors have been used to define subtypes from L1 to L9 and from T0 to T9. These subtypes span an effective temperature ( $T_{\text{eff}}$ ) range from  $\sim 2300$  K to  $\sim 750$  K and encompass the edge of the hydrogen-burning main sequence ( $T_{\text{eff}} \sim 1700$  K; L5–L6). Water (H<sub>2</sub>O) bands dominate the spectra of both Ls and Ts. However, the L dwarfs are characterized by the disappearance of the optical bands of TiO and VO (Jones & Tsuji 1997) that define the M dwarfs, the growth of near-infrared FeH and CrH features, the emergence of CH<sub>4</sub> in the *K* ( $\sim 2.0$ – $2.2 \mu\text{m}$ ) and *L'* ( $\sim 3.3 \mu\text{m}$ ) bands, and the progressive reddening of their *J*–*K* colors. The T dwarfs are distinguished by the appearance of strong CH<sub>4</sub> features in the *H* ( $\sim 1.5$ – $1.8 \mu\text{m}$ ) and the *K* bands, the weakening and disappearance of the metal

hydride features, the growing importance of collision-induced absorption by H<sub>2</sub> (Borysov & Frommhold 1990; Borysov, Jørgensen, & Zheng 1997), the strength of neutral alkali metal resonance lines shortward of 1.0 micron (Burrows, Marley, & Sharp 2000), and “anomalously” blue infrared colors. It is thought that the L/T transition is near  $\sim 1300$  K. All T dwarfs are brown dwarfs, with substellar masses, but many L dwarfs, however exotic, could be stars with masses above the main sequence edge.

While most of these trends and characteristics are understood in terms of general chemistry (Burrows & Sharp 1999; Fegley & Lodders 1996; Lodders 1999), the centrality of molecules in L and T dwarf atmospheres has put a new premium on the calculation of molecular opacities and abundances. Though theorists have gradually responded to this challenge (Partridge & Schwenke 1997; Burrows et al. 2002a; Dulick et al. 2003; Burrows & Volobuyev 2003), their remain significant deficits in the relevant molecular databases. A glaring example is the absence of data on the hot bands of methane in the *H* band, but across the board molecular spectroscopy lags the atomic spectroscopy developed over the last hundred years to support classical stellar atmosphere calculations. As a result, theoretical models of L and T dwarf atmospheres are still evolving and the extraction of physical

the growing library of well-calibrated spectra, though possible in a crude sense, remains imprecise (Burrows et al. 2002b; Marley et al. 2002; Tsuji, Nakajima, & Yanagisawa 2004; Burgasser, Burrows, & Kirkpatrick 2005).

However, the most difficult challenge confronting theorists designing models of L dwarfs and the L to T transition is the accurate incorporation of condensate clouds (*e.g.*, calcium aluminates, silicates, iron). Such refractories form at the M to L transition temperatures ( $\sim 2300\text{--}1800$  K), persist and thicken to dominate and define the L dwarfs, and when their atmospheric effects finally diminish are thereby responsible for the L to T transition (Burrows et al. 2001; Ackermann & Marley 2001; Marley et al. 2002; Tsuji, Ohnaka, & Aoki 1999). Were it not for condensate clouds the Ls would not be red in infrared colors and get redder with decreasing  $T_{\text{eff}}$ . In fact, the L dwarfs would not exist as a spectroscopic type<sup>2</sup>. Hence, to understand the M $\rightarrow$ L $\rightarrow$ T sequence and their spectra in detail requires a mastery of not only the chemical condensation sequences and the consequent elemental depletions (“rainout”; Burrows & Sharp 1999) in a gravitational field, but the spatial extent, particle size and shape distributions, grain optical properties, and meteorology of clouds as well. These complications do not confront one who models most other types of “stars.”

After the first rush of basic discoveries, observers are now beginning to refine our knowledge of L and T dwarfs from the optical to the mid-infrared. Some target facts to explain include the brightening in the  $J$  ( $\sim 1.2\text{--}1.3$   $\mu\text{m}$ ) and  $Y/Z$  ( $\sim 1.0\text{--}1.1$   $\mu\text{m}$ ) bands for the early T dwarfs (Dahn et al. 2002; Tinney, Burgasser, & Kirkpatrick 2003; Vrba et al. 2004), despite the decrease in bolometric luminosity along the spectroscopic sequence (Golimowski et al. 2004), the resurgence in the early Ts of FeH at  $\sim 0.99$   $\mu\text{m}$  (McLean et al. 2003; Burgasser et al. 2004; Nakajima, Tsuji, & Yanagisawa 2004; Cushing, Rayner, & Vacca 2005), the non-equilibrium CO abundances inferred from spectral observations at  $4.5\text{--}4.9$   $\mu\text{m}$  (Golimowski et al. 2004), the appearance of the  $2.2$   $\mu\text{m}$  and  $3.3$   $\mu\text{m}$  CH<sub>4</sub> features in the late Ls, and the narrow apparent range of  $T_{\text{eff}}$  at the M $\rightarrow$ L and L $\rightarrow$ T transitions. In fact, Golimowski et al. (2004) suggest that  $T_{\text{eff}}$  is nearly constant from L7 to T4.5. Moreover, the actual prevalence of spectroscopic binaries among the observed L and T dwarfs, and the resulting misplacements on the HR diagram, remain a concern and a caution (Liu & Leggett 2005; Gelino & Kulkarni 2005; Burgasser et al. 2005).

The brightening in the  $J$  band is the most intriguing anomaly. Its explanation must be the rapid thinning out of the clouds in the spectrum-forming region of the brown dwarf atmosphere during the L $\rightarrow$ T transition. But how the effective opacity of the silicate clouds decreases so quickly with  $T_{\text{eff}}$  and spectroscopic subtype to yield heavy-element depleted T dwarf atmospheres has yet to be explained. Ideas include the emergence of holes in the clouds, whose areal filling factor would need to increase with spectral subtype (Burgasser et al. 2004), a sudden collapse of the cloud deck (Tsuji & Nakajima 2003; Tsuji, Nakajima, & Yanagisawa 2004), or an in-

crease in the “sedimentation efficiency” of the clouds, with a concomitant rapid increase in the silicate particle size (Knapp et al. 2004). All these models have their strengths and weaknesses, and all are ad hoc, with little physical or meteorological justification for the rapid transitions proffered.

There is emerging evidence that the L and T spectroscopic sequences are not a one-parameter family in  $T_{\text{eff}}$ , but that there is a second (and, perhaps, a third) parameter. Burrows et al. (2002b) and Knapp et al. (2004) suggest that this second parameter is gravity and our calculations here lend strong support to this notion. The widths of both the L and the T dwarf regions in HR diagrams are best explained with a range of gravities. Metallicity may also play a role, but a subordinate one, except for rare outliers, and we explore in this paper the metallicity dependence of L and T dwarf model atmospheres, spectra, and colors.

In this paper, we provide a new generation of L dwarf and T dwarf model spectra, colors, and atmospheres. We use updated FeH, CrH, TiO, and VO gas-phase opacities and abundances and investigate the dependence on cloud model parameters, in particular particle size and cloud extent/shape. To do so, we have developed a sophisticated and self-consistent algorithm for handling clouds in atmosphere calculations. With this algorithm, we demonstrate the ambiguities that remain in any treatment of the L $\rightarrow$ T transition, while generating good spectral and color models for both the early- and mid-L dwarfs and the mid- and late-T dwarfs. In the process, we provide and discuss new spectral models, temperature/pressure profiles, color-magnitude diagrams, and color-color diagrams for a broad range of  $T_{\text{eff}}$ s, gravities, metallicities, and particle sizes.

In §2, we list the numerical tools and databases we have used to generate self-consistent molecular atmospheres and discuss the numerical method we employ to handle clouds and convection in L and T dwarf atmospheres. We review in §3 general cloud physics and our cloud model parametrizations. Then, we continue in §4 with a discussion of the effects of cloud shape, particle size, and gravity. The associated models are provided only to explore parameter dependences; they are not our best model results. We then introduce our baseline model, which, though manifestly limited given the current rudimentary knowledge of cloud physics and incorporating as it does simple ansatzes (as do all other published models), nevertheless gives acceptable fits to the observations outside of the problematic L9-T3 spectral range. This model suite is being provided to astronomers to aide them in understanding the rich harvest of L and T dwarf spectral data. In §5 we discuss representative temperature/pressure ( $T/P$ ) profiles that serve as the jumping-off point for further speculation on the L $\rightarrow$ T transition. Next, in §6 we provide spectra for our fiducial model set as a function of  $T_{\text{eff}}$ , gravity, and metallicity, as well as a few comparisons between our spectral models and data to establish that the models fit reasonably well. This is followed in §7 by  $M_J$  versus  $J - K$ ,  $M_K$  versus  $J - K$ , and  $M_{z'}$  versus  $i' - z'$  color-magnitude diagrams for these baseline models. For comparison, data for M, L, and T dwarfs with known parallaxes are superposed. Finally, in §8 we summarize our conclusions and discuss what

<sup>2</sup> This fact serves to emphasize that the span and importance of the L dwarf family is a function of metallicity, and for subdwarfs

## 2. NUMERICAL TOOLS AND CHEMICAL DATABASES

In a study such as the one we conduct for this paper many self-consistent spectra and atmospheres must be generated for a variety of physical parameters. To do so expeditiously, it is undesirable and expensive to calculate “on the fly” the opacities at a given wavelength from the extensive line lists available. Rather, we precompute and tabulate at 5000 frequency points, logarithmically spaced from  $0.3 \mu\text{m}$  to  $300 \mu\text{m}$ , the absorption and scattering opacities on a mesh in  $T/P$  space for  $\sim 30$  of the dominant molecular and atomic species found in L and T dwarf atmospheres. These tables are then used with a table of the corresponding molecular and atomic abundances at the desired metallicity to produce a large table of total opacities as a function of frequency, temperature, and pressure. Such a table fully incorporates the physics of line broadening and stimulated emission and is interpolated in during the iteration of the spectral/atmosphere model until a converged  $T/P$  profile and a spectrum in radiative equilibrium are obtained. Instead of requiring hours on a supercomputer to generate a model, this procedure typically requires only minutes on a single-processor workstation. To obtain spectra at higher frequency resolution, the derived  $T/P$  profile can be reused with a higher-resolution opacity table, without the need to iterate further.

The atmospheric structure is computed using a specific variant of the stellar atmospheres code TLUSTY (Hubeny 1988; Hubeny 1992; Hubeny & Lanz 1995), with modifications as described in Burrows et al. 2002b, Sudarsky, Burrows, & Hubeny (2003) and Hubeny, Burrows, & Sudarsky (2003). We have developed a computational scheme to treat clouds and their interplay with convection zones efficiently. The approach will be described in detail elsewhere (Hubeny et al., in prep.); here we briefly mention some of its most important aspects.

We have reformulated the general linearization scheme in the so-called Rybicki-type approach (Mihalas 1978), which consists in writing the global linearization (Jacobi) matrix in block form, where each block contains an individual state parameter for all depth points. This allows us to avoid using Accelerated Lambda Iteration (ALI) to treat the radiative transfer equation. Instead, we use full linearization of the radiation intensities, which leads to much faster and more stable convergence, without compromising on computer time.

Convection is treated in the mixing-length formalism, with a mixing length of one pressure scale height. In actual brown dwarf atmospheres, the temperature gradient is very close to the adiabatic gradient. During the linearization iteration, it often happens that the current gradient is somewhat lower than the adiabatic gradient, even when in reality it should be larger. We have devised a procedure that detects such spurious “convection gaps” and recomputes the temperature structure in such a way that at those points the convective flux is indeed non-zero before entering the next iteration of the linearization.

In addition to introducing a flexible way to treat cloud shapes (see §3.1), we have developed several ways to self-consistently determine the cloud’s position. It turns out that it is more stable not to recalculate the cloud position after each iteration; instead it is preferable to per-

the clouds fixed between updates. In addition, we have introduced a flexible depth-point rezoning scheme. Essentially, we place additional depth points close to the cloud base whenever the new cloud position is recalculated. Finally, in some cases the cloud position is found to oscillate between two (sometimes even three) distinct positions. This problem is avoided by setting the updated position of the cloud base between the previous position of the cloud base and the intersection of the  $T/P$  profile and the condensation curve. At convergence, the cloud base will be at the proper intersection point.

The equation of state from which we obtain the  $T/P/\text{density}(\rho)$  relation is that of Saumon, Chabrier, & Van Horn (1995). The molecular compositions and ionization fractions (Burrows, Sudarsky, & Lunine 2003) are obtained using the chemical equilibrium code SOLGASMIX (Burrows and Sharp 1999), with updated thermochemical data for Ti and V compounds, silicates and calcium aluminates,  $\text{H}^-$ , and metal hydrides. The abundance code incorporates prescriptions for rainout and depletion due to condensate formation of refractory silicates, aluminates, titanates, iron, water, and ammonia. Despite the overall complexity of the problem, the most important atoms and non-refractory molecules comprise a small subset:  $\text{H}_2$ ,  $\text{H}_2\text{O}$ ,  $\text{CH}_4$ ,  $\text{CO}$ ,  $\text{N}_2$ , and  $\text{NH}_3$ , FeH, CrH, TiO, VO, Na, and K.

Our always-evolving opacity/spectroscopy database would require a paper in itself to explain, but is partially described (with references) in Burrows et al. (1997, 2001, 2002a, 2003). The opacities of the alkali metal atoms are taken from Burrows, Marley, & Sharp (2000), which are similar in the line cores and near wings to those found in Burrows & Volobuyev (2003). For future work, we have extended the opacity database into the UV down to  $\sim 0.08 \mu\text{m}$ . Our solar-metallicity elemental abundances are taken from Allende-Prieto, Lambert, & Asplund (2002), which supercedes Anders & Grevesse (1989). Allende-Prieto, Lambert, & Asplund have found that in the past the solar abundances of oxygen and carbon were overestimated by as much as  $\sim 35\text{--}45\%$ . While this change has but subtle consequences for stellar and solar atmospheres, since the water abundance so dominant in L and T dwarf atmospheres scales almost directly with the oxygen abundance, these atmospheres are much more directly affected by the change. Using Spitzer IRAC data and our theoretical models, Patten et al. (2004) show that the new abundances fit the mid-infrared data much better. Hence, and in a curious and unexpected way, the new solar abundances are partially validated by brown dwarf observations.

Cloud physics, structure, character, and opacities play a major role in the  $\text{M}\rightarrow\text{L}$  transition, L dwarf atmospheres, and the  $\text{L}\rightarrow\text{T}$  transition and so are discussed separately in the following section.

## 3. CLOUDS AND CLOUD MODEL DESCRIPTION

In the atmospheres of late M dwarfs with  $T_{\text{eff}} \sim 2500 \text{ K}$ , the most refractory compounds start to condense. These are mostly the calcium aluminum oxides grossite ( $\text{CaAl}_4\text{O}_7 \equiv \text{CaO} + 2(\text{Al}_2\text{O}_3)$ ) and hibonite ( $\text{CaAl}_{12}\text{O}_{19} \equiv \text{CaO} + 6(\text{Al}_2\text{O}_3)$ ), among others, and first appear in the upper radiative, not the lower convective, zones. Figure 1 depicts the condensation curves of some of the most

dwarfs, L dwarfs, and brown dwarf atmospheres. As Fig. 1 indicates, this first phase of condensate cloud formation is followed, as the temperature drops, by the condensation of titanium compounds, at the expense of gas-phase TiO, and later by the condensation of VO. Therefore, the disappearance of TiO and VO lags slightly, but follows close on the heels of, the first emergence of refractory clouds. Due to the low elemental abundances by number of titanium ( $\sim 8 \times 10^{-8}$ ) and vanadium ( $\sim 10^{-8}$ ), the compounds into which TiO and VO condense (see Fig. 1) are themselves not major components of this radiative cloud layer.

In retrospect, this early transition from late M dwarfs to L dwarfs was first identified by Jones & Tsuji (1997), who for late Ms noted the near simultaneous weakening of the TiO and VO spectral features with the shallowing of the water troughs. The latter is naturally explained by the appearance of a new continuum absorber, clouds of the refractory calcium aluminates. However, though oxygen is abundant, the elemental abundances of calcium and aluminum are not, just  $\sim 2.0 \times 10^{-6}$  and  $\sim 2.8 \times 10^{-6}$ , respectively. As a result, this first generation of clouds is rather thin, though the particle sizes in radiative zones can be small ( $\sim 0.5$ – $5$  microns, Cooper et al. 2003). It is not until the appearance at slightly lower temperatures of condensates containing silicon, magnesium, and/or iron, with elemental abundances  $\sim 10$  times those of calcium and aluminum, that the areal mass density of refractory clouds can be respectable. With the lowering of  $T_{\text{eff}}$  and the appearance of condensed iron and silicates (such as forsterite,  $\text{Mg}_2\text{SiO}_4$ , and enstatite,  $\text{MgSiO}_3$ ), the photospheric layer begins to coincide both with the thickening silicate cloud layer and with a convective zone, and the pattern of the mid-L dwarf atmosphere is firmly established. Therefore, the transitions from M to L dwarf, from calcium aluminate to silicate/iron condensates, and from radiative to convective clouds overlap, though not perfectly.

As Fig. 1 indicates, at a given pressure the many condensates can appear in a narrow range of temperature. Furthermore, whatever the particle sizes and optical constants, the optical depths of such clouds are themselves sufficient after the early Ls to trip convection (and the associated updrafts and downdrafts) where there are clouds. Hence, after the early Ls (for which the first condensates inhabit a stably-stratified radiative zone) every condensate whose condensation curve intersects the dwarf's  $T/P$  profile will most probably reside in a common convection zone. It does not make sense to assume that each condensate is a separate, isolated layer, like a “pousse café.” Rather, as the  $T_{\text{eff}}$  decreases and the first clouds thicken, tripping convection in the atmosphere, condensation and grain growth will occur over the same finite time and pressure/radius range for many condensates. The kinetics of such a soup of growing condensates poses a daunting problem never before addressed, and not addressed here, though grain kinetics in the brown dwarf context has been receiving some attention of late (Helling et al. 2001, 2004; Woitke & Helling 2003, 2004). Nevertheless, the equilibrium particle size distribution, achieved through the balance of growth processes in the convective zone and grain destruction at and below the

$T/P$ -profile/condensation-curve intercept, is poorly constrained by theory (Cooper et al. 2003; Ackerman & Marley 2001). Furthermore, the optical constants of heterogeneous grains of indeterminate composition and layering are not easily derived from first principles. Qualitatively, it is clear that the modal particle size of grains in stable radiative zones is smaller ( $\sim 0.1$ – $5.0 \mu\text{m}$ ) than in turbulent convective zones ( $\sim 10$ – $150 \mu\text{m}$ ) (e.g., Cooper et al. 2003), but confidence in the current analytic estimates should not be great.

Once formed, clouds will not extend throughout the atmosphere above (to lower pressures and temperatures) the condensation intercept, but will settle into a tighter spatial distribution bounded (approximately) from below by this intercept. Hence, the upper atmosphere will be depleted of the heavy elements (such as Si, Mg, Fe, Ca, and Al) of which condensates are comprised. The T dwarfs themselves clearly indicate the general correctness of this conclusion; their clear spectra demand that their condensate clouds reside at great depths below the formation region of the emergent spectrum (Marley et al. 1996; Burrows et al. 2002b). The same is true of Jupiter and Saturn, whose atmospheres are devoid of heavy elements (Fegley & Lodders 1996), but which must house at depth ( $\sim 1000$ – $3000$  bars) both silicate and iron clouds. The oxygen fraction in an L or T dwarf is so large ( $\sim 5 \times 10^{-4}$ , solar) that condensation depletes its upper-atmospheric abundance by no more than  $\sim 15\%$  (Burrows & Sharp 1999). Below the cloud base (at higher pressures) is the “infinite” reservoir of heavy elements that extends throughout the dwarf and which sets the heavy-element abundance boundary condition at the cloud base. However, the heavy elements that may have once existed in the upper atmosphere before condensation do not all remain in the cloud once formed. How much cloud material does remain in the cloud depends on the dynamics of the cloud itself. The actual areal mass density, spatial extent, and shape of a cloud is not easily determined and depends upon the interplay of turbulent gas motions, grain growth, overshoot, turbulent and eddy diffusion, and gravitational settling, as does the grain size distribution itself. Ackerman & Marley (2001) and Cooper et al. (2003) suggest that the thickness of a cloud scales with the local pressure scale height and that the cloud material is distributed exponentially from its base with a scale height between  $\sim 0.3$  and  $\sim 1.0$  pressure scale heights. This seems reasonable, but the effect of multiple condensation intercepts for the different species and of an extended convection zone that can encompass these multiple condensation lines is not at all clear. Nor is it clear how the modal particle size varies with altitude, though there are some hints (Cooper et al. 2003).

For the time being, this state of complexity demands simple parametrizations. Our approach has been to parametrize the spatial extent and shape of the condensate cloud and to test various composite optical properties and modal particle sizes, loosely guided by extant theory and previous practice (Cooper et al. 2003; Burrows et al. 1997, 2001; Ackerman & Marley 2001; Allard et al. 2001)<sup>4</sup>. For a given parametrization, we

<sup>4</sup> For a given modal particle size, we use the Deirmendjian (1964)

have compared the resulting color-magnitude diagrams and spectra with observations in an attempt to settle on the fiducial condensate-cloud approach that can be used for our next generation of atmosphere/spectral models (published herein) for  $T_{\text{eff}}$ s from 2200 K to 700 K and a variety of gravities and metallicities, collectively encompassing the L and T dwarf ranges (This is our model E described in §3.1). Since the mid- to late-Ts are not affected by such clouds, this effort is germane only to L dwarf models and the L→T transition. In the process, we have determined the dependence of dwarf spectra and colors on particle size and cloud morphology.

### 3.1. Cloud Parametrizations

We assume that the clouds are uniformly distributed over the sphere and that there are no holes in either latitude or longitude. The position of the high-pressure base of the cloud is set at the intersection of the  $T/P$  profile and the condensation curve. The corresponding quantities are denoted by  $P_0$  and  $T_0$ , and the corresponding column mass by  $m_c$ . (The pressure at a given depth is equal to  $g \times m$ , where  $g$  is the surface gravity and the areal mass column density is  $m$ .) The opacity (per gram of atmospheric material) of a condensate  $a$  is given by

$$\kappa_a(\nu, m) = N_a M_a \frac{A_N}{\mu} S_a \sigma_a(\nu, a_0) f(m), \quad (1)$$

where  $N_a$  is the mixing ratio of species  $a$ ,  $M_a$  is its molecular weight (in grams),  $\mu$  is the mean molecular weight of the atmospheric material,  $A_N$  is Avogadro's number,  $S_a$  is the supersaturation ratio,  $\sigma_a(\nu, a_0)$  is the opacity per gram of species  $a$  for frequency  $\nu$  and modal particle size/radius  $a_0$ , and  $f(m)$  is our cloud shape function, defined such that the full presence of a cloud is denoted by  $f = 1$  while its complete absence is denoted by  $f = 0$ .

$N_a$  and  $M_a$  are taken as known quantities (depending on the assumed composition and varying with metallicity). The supersaturation parameter and the modal particle size are taken as input parameters of the model; for iron  $S_a$  is 0.01 and for the silicates such as forsterite it is 1.0. The cross sections for both true absorption and scattering are taken from precalculated Mie tables, interpolating to the assumed particle size  $a_0$ .

In the absence of an ab-initio theory of cloud formation and merger, we envisage a simple empirical model of a composite cloud having a flat part just below the intersection point (upper cloud deck), and having an exponential decline on the both sides of this flat part. The extent of the flat part, and the exponents of the decline on both sides are free parameters of the problem. The cloud shape function is thus given by

$$\begin{aligned} f(m) &= (m/m_1)^{s_1}, & m &\leq m_1, \\ f(m) &= 1, & m_1 &\leq m \leq m_0, \\ f(m) &= (m/m_0)^{-s_2}, & m &\geq m_0, \end{aligned} \quad (2)$$

where  $m_1$  and  $m_0$  are the upper (low-pressure) and lower (high-pressure) boundaries of the flat part of the cloud.  $s_1$  and  $s_2$  are indices such that  $1/s_1$  and  $1/s_2$  times the local pressure scale heights are the scale heights of the particle number distributions in the exponential tails.  $m_1$  can be parameterized in different ways. For a single isolated cloud species,  $m_c$  would naturally be  $m_c$  and

pressure scale height would indicate the cloud's approximate extent. However, for multiple cloud condensates with a range of  $T_0$ s that inhabit a convectively mixed region, the flat portion should encompass the multiple cloud  $T/P$  intercept points, with an extent roughly indicated by the thickness of the condensate band in Fig. 1. This is why we have introduced the flat portion in eq. (2).

To study the influence of the cloud shape function on the temperature structure and the predicted spectra, we have considered the following five cases. In model A, the cloud declines exponentially below the high-temperature intersection point, but extends upward all the way to the surface ( $s_1 = 0$ ;  $s_2 = 10$ ). Model B corresponds to having the cloud everywhere in the atmosphere ( $s_1 = 0$ ;  $s_2 = 0$ ). Models A and B are similar and roughly correspond to the ‘‘Dusty’’ models of Chabrier et al. (2000) and Allard et al. (2001).

Model C corresponds to a cloud decaying above and below the intersection point without having a flat part ( $s_1 = 6$ ;  $s_2 = 10$ ); model D represent a cloud that decays above the intersection point ( $s_1 = 6$ ), while extending all the way down deep into the dwarf ( $s_2 = 0$ ); and, finally, model E corresponds to our generic, fiducial cloud – a cloud with a flat part between the intersection point of one of the most refractory condensates (such as grossite) and the intersection point for one of the less refractory condensates (such as forsterite), and exponential decays on both sides ( $s_1 = 6$ ;  $s_2 = 10$ ).  $s_1 = 6$  is steep, but comports with the expected thinness of single clouds of refractory condensates having large particle radii. Models E and D are similar.

Our default value of  $m_0$  for the composite cloud model E is where  $T_0$  for the most refractory condensates (the calcium aluminates) equals the atmospheric temperature. For simplicity, in our fiducial model E we have set  $T_0$  equal to a constant 2300 K (Fig. 1). Our  $m_1$  for all models is taken to coincide with the intercept with the forsterite condensation curve (the forsterite  $m_c$ , at a temperature between 1500 and 1900 K; see Fig. 1).

Hence, the remaining parameters of our cloud models are the modal particle radius ( $a_0$ ), and the optical properties of the representative condensate. We have studied the consequences of using enstatite, corundum, and forsterite for the latter and have settled on forsterite ( $\text{Mg}_2\text{SiO}_4$ ) for this generation of dwarf models. Its abundance should be one of the largest in the mix, and, as we will see (§6), when the particle radii are near  $\sim 50$ – $100 \mu\text{m}$ , the spectral fits over most of the relevant  $T_{\text{eff}}$  and gravity range are rather good.

## 4. EXPLORATION OF PARAMETER DEPENDENCES

To clarify the role of cloud extent as described in §3.1, Fig. 2 compares theoretical spectra for cloud distribution models A, B, C, D, and E at  $T_{\text{eff}}$ s of 1100 and 1700 K, a gravity ( $g$ ) of  $10^5 \text{ cm s}^{-2}$  and a modal particle radius of  $30 \mu\text{m}$ . This figure does not represent our preferred set of models, but rather is meant to portray the generic differences between the cloud models described in §3.1. At  $T_{\text{eff}} = 1100 \text{ K}$ , models C, D, and E are very similar, since the cloud base where these models differ is all but invisible for this  $T_{\text{eff}}$ . These models also maintain the large contrast observed for this  $T_{\text{eff}}$  range between the water

band peaks. Models A and B, which allow the cloud to extend to the lowest pressures, are severely affected by the cloud opacity, and result in very flat spectra and a redistribution of flux from short to long wavelengths that is completely inconsistent with observations (see §6). On the bottom panel of Fig. 2, we show the corresponding models for  $T_{\text{eff}} = 1700$  K. Here, the near degeneracy between models C and D/E is broken and for model C we can discern in the stronger  $J$  and  $H$  peaks the absence of cloud below the forsterite condensation curve. Clearly, the extent of the cloud(s) does make a difference.

In Fig. 3, we compare models A, B, C, D, and E for 30- $\mu\text{m}$  particles on an  $M_J$  versus  $J - K$  color-magnitude (HR) diagram, but for a wider range of  $T_{\text{eff}}$ s than provided in Fig. 2. Included are both the cloud-free (clear) curve and a collection of measured M, L, and T dwarfs with parallaxes. All the cloud models (except model A) reproduce the general behavior of the M $\rightarrow$ L transition and the C, D, and E models comfortably inhabit the early-to-mid L dwarf regime. The presence of clouds clearly defines the Ls. In addition, models C, D, and E are degenerate below  $T_{\text{eff}} \sim 1400$  K at this gravity and reach the measured mid-T dwarf region to the blue in reasonable fashion. Note that the extended cloud models A and B never make the transition to the “clear” behavior of the late T dwarfs and they are off in  $J - K$  by as much as 3 magnitudes at low  $T_{\text{eff}}$ . However, though as Fig. 2 demonstrates the corresponding spectra for models A and B are disfavored, even these models transverse the L-type spectral band in reasonable fashion. The same can be said for the models of Chabrier et al. (2000) (to which models A and B are closest in their particulate spatial distribution) for  $M_J$ s from  $\sim 11$  to  $\sim 14.5$ . However, depending upon the isochrone chosen, the Chabrier et al. models later than  $\sim 15.0$  magnitudes are redder than models A and B by as much as  $\sim 0.5$  to  $\sim 2.0$  magnitudes. This is in part a consequence of their use of an ISM particle size distribution.

Furthermore, and importantly, as shown in Fig. 3, the observations of early- to mid-T dwarfs indicate a substantial brightening in  $J$ , peaking near T3. If in fact this observational trend is denoting brightening along an evolutionary track or along a near-constant gravity/metallicity trajectory, and not an incompletely sampled scatter in the known population of brown dwarfs with parallaxes or the effects of binarity, then models C, D, and E, though they handle the early-to-mid Ls and the mid-to-late Ts reasonably well, do not adequately reproduce the L $\rightarrow$ T transition region. The diminution of the effects of cloud optical depth with decreasing  $T_{\text{eff}}$  is occurring more rapidly in the real objects than in the models. We will discuss this more in §5 and §8.

Figure 4 portrays the dependence on the exponential cutoff parameter,  $s_1$ , of the theoretical spectrum of an L dwarf with a  $T_{\text{eff}}$  of 1500 K, a gravity of  $10^5 \text{ cm s}^{-2}$ , a modal particle radius of 30  $\mu\text{m}$ , and the model E particle density distribution. The purpose of this diagram is to demonstrate that the upper (low-pressure) particle density scale height, a quantity that is very loosely constrained by first principles and that may be chosen by modelers with little physical motivation, makes a difference of as much as  $\sim 20\%$  in the near infrared fluxes. Ignorance of this quantity can translate into a further am-

the  $s_1$  the thinner the upper cloud deck. For our subsequent model E spectra, we chose  $s_1 = 6$  to reflect our prejudice that the refractory clouds made up of large particles settle more compactly than terrestrial water clouds (Ackerman & Marley 2001).

Next, we portray in Fig. 5 an HR diagram similar to Fig. 3, but as a function of modal grain particle size/radius from 3 to 100 microns. For comparison, the cloud-free trajectory is included.  $T_{\text{eff}}$ s from 700 K to  $\sim 2000$  K are represented (see caption) and model E with  $s_1 = 6$  is employed. A constant gravity of  $10^5 \text{ cm s}^{-2}$  and forsterite optical properties are assumed. Data for M, L, and T dwarfs with known parallaxes are superposed.

Figure 5 shows that, at least in  $M_J/(J - K)$  space, particle size makes little difference for the early- to mid-L dwarfs, but a very large difference in the turnaround elbow and in the  $M_J$ s for the early- to mid-T dwarfs. The trajectory with a larger particle size approaches the anomalous T3 brightness, but fails to include the latest, reddest L dwarfs. A small particle size can “fit” the latest L dwarfs, but completely misses the early T dwarfs. In short, all else being equal no one particle size and gravity combination can be made to fit all the data, even from the perspective of this lone HR diagram. One might conclude from Fig. 5 that a systematic increase in  $a_0$  with decreasing  $T_{\text{eff}}$  might be indicated (Knapp et al. 2004), but how this is accomplished by nature would remain to be determined. In fact, the simple convective cloud models of Cooper et al. (2003) and Ackerman & Marley (2001) predict that particle size slowly decreases with decreasing  $T_{\text{eff}}$ . However, a fast transition to large particles as  $T_{\text{eff}}$  decreases, or at some critical  $T_{\text{eff}}$ , due perhaps to the onset of runaway particle growth and precipitation in convective flows with large shears (Shaw 2003; Kostinski & Shaw 2005), would be worth investigating.

However, as is demonstrated by Fig. 6 for a set of  $T_{\text{eff}} = 1500$  K and  $g = 10^5 \text{ cm s}^{-2}$  models as a function of modal particle radii and by a basic knowledge of L dwarf spectra (as well as of the figures in §6), small particle sizes below  $\sim 30$  microns result in theoretical spectra that are much too smooth, that don’t provide the high contrasts across the water bands generically observed for objects later than mid-L dwarfs, that suppress the K I doublet in the  $J$  band, and that ruin the CO and methane fits between 2.2 and 2.4 microns. Hence, small values for  $a_0$  are strongly disfavored for L and T dwarf models. The upshot is that while larger particles ( $> 40 \mu\text{m}$ ) seem favored from general spectral considerations, they make fitting the reddest late L dwarfs problematic. From now on, we will take  $a_0 = 100 \mu\text{m}$  for our model E (with  $s_1 = 6$ ) calculations as the best representative parameter combination and see where that can lead us.

In picking a single particle size for our reference model, we are not only acknowledging, as we hope others would also do, our current ignorance of the physics and systematics of clouds in brown dwarf atmospheres, but our observation that such large particle sizes, whatever the grain kinetics, are favored by the data. We find in fact, as the following sections show, that our baseline model fits the data rather well, and certainly no worse than any other model now in the literature. The reader is invited to review the dependences on the various cloud param-

limitations of our baseline model.

A cloud model must provide the values and systematics with composition,  $T_{\text{eff}}$ , and gravity of the modal particle size, the particle size distribution, the spatial distribution (with altitude) of cloud properties, the optical constants of all the relevant grains as a function of wavelength (with the effects of grain mantling), the effects of grain asphericity, the patchiness of the clouds, the effects of convective overshoot, and the variations with longitude and latitude. Though there have been some good starts at framing the discussion of some of these components (Helling et al. 2001, 2004; Woitke & Helling 2003, 2004; Ackerman & Marley 2001; Cooper et al. 2003), we believe these issues are still to be adequately addressed. Therefore, in this paper we provide our parameter study and a phenomenological reference model, avoiding what does not work, while being guided by what seems to, all without pretending to have achieved an understanding of cloud and dust physics.

Note that the small abundances of the calcium/aluminium refractories formed in the radiative zone near the M→L transition, coupled with the higher per particle opacities of the small particles expected in such zones, result in a total optical depth that is coincidentally comparable to that for the 100-micron forsterite particles assumed in our baseline model. Hence, the total optical depth of large particles of high-abundance species (such as forsterite) can crudely mimic the total optical depth of the smaller/low-abundance particles expected in radiative zones.

Before we transition to a discussion of our fiducial dwarf model set, we present in Fig. 7 the dependence on gravity of  $T_{\text{eff}}$  trajectories in  $M_J$  versus  $J - K$  space (for  $a_0 = 30, 100 \mu\text{m}$ ). Each color represents a different gravity (either  $10^{4.5}$ ,  $10^{5.0}$ , or  $10^{5.5} \text{ cm s}^{-2}$ ), with the larger gravities to the left. For each color, the line to the left is the larger particle size ( $100 \mu\text{m}$ ).

The range of gravities employed for Fig. 7 represents a reasonable range of dwarf masses, from  $\sim 15 M_J$  to  $\sim 70 M_J$  (Burrows et al. 1997). That this range of gravities nicely covers the data points in both the L and T dwarf regimes strongly suggests that the observed widths of the L and T dwarf bands are explained by gravity variations, that  $g$  is the “second parameter.” Though one is still unsure about the latest Ls and the brightening in  $J$  near T3, this conclusion seems reasonable and has also been reached by Burrows et al. (2002b) and Knapp et al. (2004) using different arguments. However, it is still possible that binarity can be a factor in the width of the L and T spectral bands in the HR diagrams.

## 5. TEMPERATURE/PRESSURE PROFILES

Now that we have explored various cloud parametrizations, and settled upon one of them to comprise our default set (model E, with  $a_0 = 100 \mu\text{m}$ ,  $s_1 = 6$ , and forsterite’s complex index of refraction versus wavelength behavior), let us return to a discussion of the regions and structure of the generic L or T dwarf atmosphere. To do this, we provide in Figs. 8 and 9 temperature/pressure profiles for different  $T_{\text{eff}}$ s spanning the L and T dwarf  $T_{\text{eff}}$  range, at gravities of  $10^{4.5} \text{ cm s}^{-2}$  and  $10^{5.0} \text{ cm s}^{-2}$ , respectively. The red regions are convective, the dots accentuate the convective boundaries, and the as-

of the average photosphere. The dashed lines indicate the approximate positions of the inner and outer cloud boundaries, as described in §3.1.

As Figs. 8 and 9 show, at  $T_{\text{eff}}$ s from 2200 K to 1900 K clouds are radiative and the photospheres are in the radiative zone. At lower  $T_{\text{eff}}$ s, from  $\sim 1800$  K to  $\sim 1600$  K, the precise value of which depends upon gravity (and, in fact, particle size and metallicity), an isolated outer convective zone emerges that coincides approximately with the position of the condensate cloud. The increasing opacity of the particulate matter trips local convection, but at the same time flattens the T/P profile below this zone at slightly greater pressures. The upshot is an isolated radiative zone between two convective zones. Eventually, near  $\sim 1600$  K for the default model depicted here, the two convective zones merge. What happens meteorologically and dynamically when they merge might make for an interesting study; we will return to this later. After the two convective zones merge, the outer convective boundary is always near 1500–1600 K and ranges in pressure from  $\sim 0.5$  to  $\sim 20$  bars for the lower gravity and from  $\sim 1$  to  $\sim 80$  bars at the higher gravity. As Figs. 8 and 9 demonstrate, the pressures at the cloud base for the two model sets range from  $\sim 0.3$  to  $\sim 20$  bars for  $g=10^{4.5} \text{ cm s}^{-2}$  and from  $\sim 0.7$  to  $\sim 100$  bars for  $g=10^{5.0} \text{ cm s}^{-2}$ . At a given atmospheric temperature, increasing gravity or decreasing metallicity increases the local pressure. Centered at a gravity of  $10^5 \text{ cm s}^{-2}$  and solar metallicity, at a given  $T$  a one order of magnitude range in either gravity or metallicity translates into a variation of about an order of magnitude in pressure.

The fact that the pressures at the cloud base inexorably rise with decreasing  $T_{\text{eff}}$  implies that the optical depth of the cloud increases dramatically with decreasing  $T_{\text{eff}}$ , all else being equal. The Rosseland optical depth of the condensate clouds in the models in Figs. 8 and 9 range from of order unity to one hundred. The clouds get thicker with later spectroscopic type from the early L dwarfs to the late T dwarfs.

However, as the positions of the asterisks indicate, the photosphere ranges from  $\sim 0.2$  to  $\sim 0.6$  bars at the lower gravity and from  $\sim 0.5$  to  $\sim 2.0$  bars at the higher gravity. Its position is tightly constrained to lie in a narrow pressure range around a bar. As a result, it recedes from the cloud base and cloud tops with decreasing  $T_{\text{eff}}$ ; as Figs. 8 and 9 demonstrate, the top of the convective zone is progressively buried and separates from the “photosphere.” This is the origin of the waning influence as  $T_{\text{eff}}$  decreases of clouds in dwarf atmospheres and spectra. Note that as  $T_{\text{eff}}$  decreases, the photosphere is first in a radiative zone (early L), then the convective zone (mid L), and finally in the outer radiative zone. Figure 10 depicts the Rosseland depth above the clouds due to gas as a function of  $T_{\text{eff}}$  for various gravities and shows how as  $T_{\text{eff}}$  decreases the cloud tops are more and more obscured by the cloud-free, gas-dominated regions.

On the basis of the discussion above, one might conclude that the L dwarfs, the transition from L to T, and the brightening in the  $J$  band depicted by the data plotted on Figs. 3, 5, and 7 all naturally follow and can be explained by the phenomenology represented in Figs. 8 and 9, and most of this is true. However, the L→T transition appears to occur much more quickly than in our

from the photosphere, or the particle size increases, faster than is implied by the models of Figs. 8 and 9, whatever their other strengths. It has been suggested that the clouds break up and spawn holes that widen with decreasing  $T_{\text{eff}}$  (Burgasser et al. 2004). Since the clouds inexorably thicken as  $T_{\text{eff}}$  decreases, we do not favor this break up hypothesis. However, given our current ignorance of cloud meteorology, dynamics, and grain growth, not the least at the cloud tops that for late-L and early-T dwarfs are closest to the photospheres, we can not at present eliminate this scenario. Be that as it may, we can compare the spectral and color models we derive with representative observed dwarf spectra to conclude that apart from the issue of the L→T transition, our new models reproduce the observations rather well. Next, we demonstrate this, using only the coarse model set in  $T_{\text{eff}}$  and gravity space we have generated for this paper.

## 6. SPECTRAL COMPARISONS

Figures 11, 12, and 13 summarize the spectra in the optical and near infrared associated with our baseline model set as a function of  $T_{\text{eff}}$  (Fig. 11, at solar metallicity), gravity (Fig. 12, for our three gravities), and metallicity (Fig. 13, for three metallicities)<sup>5</sup>. These models fully incorporate an algorithm for condensation clouds and the latest gas-phase opacities. As Fig. 13 indicates, and as one would generally expect, lower metallicity models are bluer (compare the green, red, and blue curves at the  $Y/Z$ ,  $J$ , and  $H$  peaks). However, some of the non-monotonic behavior in, for instance, the  $K$  band can be explained by the fact that the CO/CH<sub>4</sub> ratio, the atmospheric pressures, and the contribution of clouds are all metallicity-dependent, sometimes in countervailing ways.

In addition to incorporating the evolving effects of grains as  $T_{\text{eff}}$  decreases, these spectral models track the transition from CO to CH<sub>4</sub>, particularly manifest in the  $K$  band in the 2.3  $\mu\text{m}$  to 2.2  $\mu\text{m}$  switch, the deepening of the methane feature in the  $H$  band, the appearance (then disappearance) of FeH and CrH features near  $\sim 1.0 \mu\text{m}$  and  $\sim 0.85 \mu\text{m}$ , the emergence of the neutral Na, K, Cs, and Rb alkali features below 0.9  $\mu\text{m}$ , the emergence of the  $Y/Z$  band peak (near 1.05  $\mu\text{m}$ ), the disappearance of TiO and VO, and the resculpting of the  $J$ ,  $H$ , and  $K$  bands. The shape change in the  $K$  band due in part to collision-induced H<sub>2</sub> absorption is particularly striking. Also seen is the evolution of the K I features in the  $J$  band near 1.25  $\mu\text{m}$  and near 1.17  $\mu\text{m}$ .

Without attempting detailed fits, we compare in Figs. 14 and 15, the closest representatives of our model set at solar metallicity with four observed spectra for the L1 dwarf 2MASS J03454316+2540233 (Kirkpatrick et al. 1997; Leggett et al. 2001), the L5 dwarf SDSS J05395199-0059020 (Leggett et al. 2000; Geballe et al. 2002), the T4.5 dwarf SDSS J02074248+0000562 (Tsvetanov et al. 2000; Geballe et al. 2002), and the T8 dwarf Gliese 570D (Burgasser et al. 2000; Geballe et al. 2001). All the measured spectra are for objects with measured parallaxes (Vrba et al. 2004) and Figs. 14 and 15 are *absolute*, not relative, comparisons. Had we generated a new set of models with a finer gravity,  $T_{\text{eff}}$ , and metallicity grid, we could have obtained even better fits, but

have left that exercise to a future paper.

For the L1 dwarf 2MASS J0345, though the  $H$ -band comparison is slightly problematic, the correspondence between theory and observation in the shape of the spectrum from 1.8 to 2.3  $\mu\text{m}$  and in the  $J$  band is quite good. For the L5 dwarf SDSS J0539, the correspondence throughout the spectrum depicted is excellent, and even the FeH Wing-Ford feature at  $\sim 0.99 \mu\text{m}$  is reasonably well reproduced. Except for shape discrepancies in the  $H$  and  $K$  bands, the correspondence between theory and observation from 0.9  $\mu\text{m}$  to 1.6  $\mu\text{m}$  for the T4.5 SDSS J0207 is striking. Furthermore, for the T8 dwarf Gliese 570D, except for deviations at the  $Y/Z$  peak and in the  $H$  band (the latter due, again, to problems with the extant methane database), the “fit” with theory is remarkable. Note that all these comparisons are being made for spectra plotted linearly, not in the logarithm, and are, therefore, that much more encouraging.

The successes for the L dwarf comparisons seen in Fig. 14 suggest that for the early to mid-L dwarfs our condensation cloud model is rather good, surprisingly so given the possible variations on cloud modeling. Furthermore, Fig. 15 suggests that for the mid- to late T dwarfs the models are also good. For all four representative dwarfs depicted, the  $T_{\text{eff}}$ s and gravities shown on the plots are useful first guesses for these quantities. As Marley, Cushing, & Saumon (2004) suggest, for T dwarfs later than about T5 we find that the clear models without any direct effects of clouds fit the observations in the near to mid-infrared slightly better than the cloudy models. Marley, Cushing, & Saumon (2004) claim that this demarcation is near  $T_{\text{eff}}$ s of 1200 K. However, we determine that the effects of clouds, particularly from the optical to  $\sim 1.1$  microns (Burrows et al. 2002), completely disappear at  $T_{\text{eff}}$ s cooler than  $\sim 1100$  K. This slight difference highlights the problems that attend the L→T transition. Beyond  $T_{\text{eff}}$ s of 1100 K we discern little difference at any wavelength for which comparisons can be made between the Marley, Cushing, & Saumon (2004) models and the models presented in this paper.

## 7. COLOR-MAGNITUDE RESULTS

If there were to be a brightening due to the diminution of the effects of clouds, it is not surprising that this would be most manifest in the  $J$  and  $Y/Z$  bands. Figure 16 provides a comparison between the forsterite and the solar-metallicity gas opacities for two particle sizes and a typical atmospheric thermodynamic point. The gas-phase opacities show the classical variation due to the water absorption troughs that define the near infrared photometric bands. At  $\sim 1.05 \mu\text{m}$  and  $\sim 1.25 \mu\text{m}$ , the grain opacities are most competitive with the gas, indicating clearly that it is in the  $Y/Z$  and  $J$  bands that the recession to depth, thinning, or disappearance of the clouds would first be obvious. Hence, it is all the more perplexing that our default models can not reproduce the  $\sim 1.0$  magnitude rise seen in  $M_J$  versus  $J - K$  near subtype T3, if “rise” it is. Nevertheless, it is instructive to see just what the new models do predict. Figure 17 is a  $M_J$  versus  $J - K$  HR diagram with  $T_{\text{eff}}$  trajectories for all our fiducial models for the three gravities ( $10^{4.5}$ ,  $10^{5.0}$ , and  $10^{5.5} \text{ cm s}^{-2}$ ) and three metallicities ( $[\text{Fe}/\text{H}] = \{-0.5, 0, +0.5\}$ ). The cloud free models and the mas-

<sup>5</sup> The color-magnitude diagrams in this paper are based on the models shown in Figs. 11, 12, and 13.



also included on the plot. A given color denotes a given metallicity, the leftmost models being the most metal-poor. The green curves are for solar metallicity. For a given triplet, the leftmost model is the highest gravity.

Consonant with the discussion in §4, the early to mid-L dwarfs and the mid- to late-T dwarfs fit quite well. The thicknesses of both the T and L dwarf bands are well recreated by variation in gravity, with perhaps a slight metallicity dependence. The gravity dependence in the L→T transition is expected to be weak, while the metallicity dependence is strong, as large as could be produced by a variation in particle size of a factor of ten. The latest L dwarfs are still outliers in the theory, for all  $T_{\text{eff}}$ s, gravities, and metallicities. It is indeed ironic that to put models among these latest L dwarfs requires higher cloud opacities, while to explain the anomaly near T3 requires lower cloud opacities, emphasizing that the swing from L9 to T3 is very rapid, even more rapid than the discussion and plots in §5 provide for.

As Fig. 17 indicates, we could fit the  $J$  “brightening” around T3 with lower metallicities, only a factor of  $\sim 3$  below solar. However, as Fig. 17 also indicates, such a metallicity, though it might help with some T dwarf fits, is not consistent with most of them. Furthermore, if the observed trajectory from L to T is not very incomplete, then the metallicity explanation would be hard-pressed to explain the empty regions in  $M_J/(J - K)$  space that should be occupied by low-metallicity dwarfs.

The corresponding diagram for  $M_K$  versus  $J - K$  (Fig. 18) is more encouraging, with the green solar-metallicity lines inhabiting the L dwarf, the L→T transition, and the T dwarf regions rather well. However, the latest L dwarfs are still left out. Note that Figs. 17 and 18 suggest that the low-metallicity ( $[\text{Fe}/\text{H}] \leq -1.0$ ) subdwarf L dwarfs will swing to the blue earlier than solar-metallicity L dwarfs and, hence, that the extent of the subdwarf L dwarf family in color and  $T_{\text{eff}}$  space will be smaller. At low enough metallicity, the L dwarfs might altogether disappear as a class.

Figure 19 depicts the  $J - H$  versus  $H - K$  color-color diagram for a subset of the new models and explains a curious behavior. As before, each line is for a given gravity and all models are for solar metallicity. Data for T, L, and M dwarfs and a cloud-free trajectory (orange) are also shown. As the data indicate, there is a distinct clump of M dwarfs. To the red in both colors can be found the L dwarfs, also as a clump. However, the T dwarfs are found on the opposite side from the L dwarfs, re-traversing the M dwarf realm and extending to the blue. The clear models do not extend redward of the M dwarfs. However, the cloudy models do show this behavior, curling up to the L dwarfs, then back through or near the M dwarfs, and on to the blue T dwarfs. This sinus behavior is a consequence of the appearance, then disappearance of the clouds from the photosphere. The best fit is for models (the dashed curves) for which the  $\text{CH}_4$  opacity in the  $H$  band has been artificially increased by a factor of 2 to account for the missing  $\text{CH}_4$  hot bands. Our default model set does not incorporate this artificial enhancement, but we present such models here to show the better fits that are possible with the same opacity increase as is required for better spectral fits to measured T dwarfs in the  $H$  band

versus  $T_{\text{eff}}$  trajectories for a variety of metallicities and gravities. The basic behaviors of the entire M, L, and T dwarf families are encapsulated here, though the slope from the late L dwarf bump to the T dwarfs at lower  $T_{\text{eff}}$ s is too shallow to explain the anomalous brightening in  $J$ .

Finally, in Fig. 21 we portray model trajectories for the various metallicities and gravities of our new model set in the  $M_z'$  versus  $i'-z'$  color-magnitude diagram<sup>6</sup>. L and T dwarf data from Knapp et al. (2004) and for which there are parallaxes are superposed. The theory makes a passable job at following the dwarf points, though for the few T dwarfs included a better fit is indeed with the lower metallicity lines, while for the latter L dwarfs a slightly higher metallicity would be preferred. More data in these bands for dwarfs with parallaxes is clearly needed.

Figures 11 through 21 represent a new generation of models and the degree to which they reproduce current L and T dwarf data. All in all, the new models are an advance and they can be used with profit to extract physical information from observed spectra, particularly for the early- to mid-L dwarfs and the mid- to late T dwarfs. However, a number of questions remain unresolved, in particular the character of the  $J$  band brightening and reason for the redness and dimness of the latest L dwarfs.

## 8. CONCLUSIONS AND DISCUSSION

Using an updated gaseous opacity database and a model for clouds in L and T dwarf atmospheres, we have generated and presented a new series of spectral models spanning the  $T_{\text{eff}}$  range from 2200 K to 700 K, as a function of gravity and metallicity. The correspondence with observed spectra and infrared colors for early- and mid-L dwarfs and for mid- to late-T dwarfs is good. We find that the width of both the T and L dwarf branches is naturally explained by reasonable variations in gravity and, therefore, that gravity is indeed the “second parameter” of the L/T dwarf sequence,  $T_{\text{eff}}$  being the first. We have explored the dependence of theoretical dwarf spectra and HR diagrams upon various cloud parametrizations, such as particle size, cloud scale heights, and spatial distribution. The results are a cautionary tale that our current ignorance of detailed cloud meteorology renders ambiguous the extraction of various physical quantities such as  $T_{\text{eff}}$  and gravity for mid-L to early-T dwarfs. We estimate that errors of  $\sim 50$ – $100$  K in  $T_{\text{eff}}$  and  $\sim 0.3$  in  $\log_{10} g$  are likely, particularly near  $T_{\text{eff}} \sim 1100$ – $1500$  K. Nevertheless, for decreasing  $T_{\text{eff}}$ , we capture with some accuracy the transition from CO to  $\text{CH}_4$  in the  $K$  band, the FeH and CrH features at  $\sim 1.0 \mu\text{m}$  and  $\sim 0.85 \mu\text{m}$ , the emergence of the neutral Na, K, Cs, and Rb alkali features, the growth of the  $Y/Z$  band peak, the disappearance of TiO and VO in L dwarfs, the transformations of the  $J$ ,  $H$ , and  $K$  bands, and the evolution of the K I features near  $1.25 \mu\text{m}$  and near  $1.17 \mu\text{m}$ . Moreover, we speculate that the subdwarf branch of the L dwarfs will be narrow, and, that for low enough metallicity, the L dwarfs will disappear altogether as a spectroscopic class. Furthermore, we note that the new, lower solar oxygen abundances of Allende-Prieto, Lambert, & Asplund (2002) produce better fits to brown dwarf data than do the older Anders & Grevesse (1989) values. How-

ever, we do not reproduce the “brightening” in  $J$ , nor the dimness of the latest L dwarfs.

What could be the reason for the problems near T3 and L8/9? The  $J$  and  $Y/Z$  band brightening will require a more rapid decrease in atmospheric cloud opacity than occurs naturally in all the uniform cloud models published to date, including our own. Those of Tsuji, Nakajima, & Yanagisawa (2004) (their “UCM” set) do not reproduce either anomaly – neither do the models of Ackerman & Marley (2001), Marley et al. (2002), Chabrier et al. (2000), or Allard et al. (2001). Burgasser et al. (2004) have postulated the break up of the clouds near a  $T_{\text{eff}}$  of 1200–1300 K and the appearance of holes, whose filling fraction increases across the L→T transition until that fraction is unity. A virtue of this model is the natural explanation of the apparent resurgence of the FeH features in the early- to mid-T dwarfs (Burgasser et al. 2004; McLean et al. 2003; Cushing, Rayner, & Vacca 2005). The FeH abundances near the photospheres should be waning; holes could allow us to see more deeply to the higher-temperature regions in which the FeH abundance is large. The break-up model might imply larger temporal variations in the FeH,  $J$ , and  $Y/Z$  band fluxes for early-T and late-L dwarfs, and such variations can be looked for. However, no one has yet provided a plausible physical explanation for this break-up behavior, and the inexorable thickening of the cloud material with decreasing  $T_{\text{eff}}$  would seem (superficially?) to mitigate against this. Curiously, the interplay between rapid rotation and silicate clouds for some critical parameter regimes might result in banding, such as is seen in the atmosphere of Jupiter, and this may be playing a role in the observed  $J$ -band brightening. However, how such a cloud-rotation coupling could affect a transition from profound cloud opacity to full clarity is not immediately obvious. Be that as it may, the problem of fitting the latest L dwarfs on the infrared HR diagrams, while simultaneously also fitting their spectra, is not explained at all by the filling factor hypothesis<sup>7</sup>. In fact, it might exacerbate it.

It could be that the anomalous brightenings in  $J$  and  $Y/Z$  are the result of crypto-binarity. The binary fraction of T dwarfs is not negligible and  $\sim 0.75$  mag. ( $2.5 \times \log_{10} 2$ ) is near the magnitude of the few excesses measured. It could also be, as we show in Figs. 17, that low metallicity is the culprit. However, both explanations seem rather ad hoc and do not explain the gaps and empty regions in the  $M_J/(J - K)$  HR diagram currently inferred. The redness and low  $J$ -band fluxes seen for the latest L dwarfs might be explained by errors in the parallaxes or photometry. These objects might also be explained by supersolar metallicities. However, both these explanations seem unlikely, particularly given the large number of L dwarfs that now inhabit that region of phase space.

We have shown that when calcium-aluminate, silicate, and Fe clouds first form they do so in the radiative re-

gion, that as  $T_{\text{eff}}$  decreases an isolated convective zone emerges, and that for even lower  $T_{\text{eff}}$ s the two convective zones join. It remains to be seen what happens to the particle sizes and cloud morphology when these regions merge. Shaw (2003) and Kostinski & Shaw (2005) investigate the dependence of runaway droplet growth and rainout on the presence in convective clouds of large velocity shears and on intermittency in the turbulence. Could the merger of the outer convective cloud with the inner convective zone lead to regions of such large shears, in which particle growth on the timescales available is more rapid, and, hence, to very large particles? Could the merger lead to the irreversible partial flushing of cloud material into the interior? After the joining of the convective zones, is the timescale for grain growth too long for the convecting feedstock to avoid being dragged into the hot interior before forming opaque grains? Is a critical  $T_{\text{eff}}$ /gravity threshold for rapid grain coalescence and growth reached, beyond which the average particle is too large to contribute significant opacity (Liu, Daum, & McGraw 2005)? Or does the scale height of the silicate cloud collapse at some  $T_{\text{eff}}$  threshold? The answers to these questions require a multi-dimensional approach both to grain kinetics and growth and to convective cloud structures and motions, all properly coupled.

Since the discovery of Gleise 229B ten years ago, theorists have made great strides in modeling brown dwarf atmospheres and spectra. The thermochemical and spectroscopic data for the relevant molecules have improved considerably, as have the codes needed to handle stratified atmospheres. Observers have identified whole new spectroscopic classes, and the observations have gotten spectacularly better across the electromagnetic spectrum. Despite this palpable progress, much remains to be done. Foremost are the creation of physically-motivated cloud models, the expansion of molecular line lists that even now remain incomplete, the discovery of what lies beyond the T dwarfs at still lower  $T_{\text{eff}}$ s, the further calibration of evolutionary and spectral models with well-calibrated spectra, and the discovery and characterization of more eclipsing systems. Robust gravity and metallicity diagnostics need to be determined and pursued and the binary statistics of substellar-mass objects need to be put on a firm foundation. We look forward to participating in the next generation of progress on these problematic, yet fascinating, objects that have only recently emerged from nowhere to reawaken stellar astronomy.

The authors thank Mike Cushing, Adam Burgasser, Bill Hubbard, Jonathan Lunine, Christopher Sharp, Jim Liebert, Drew Milsom, Curtis Cooper, and Jonathan Fortney for fruitful conversations and/or help during the course of this work, as well as NASA for its financial support via grants NAG5-10760, NNG04GL22G, and NNG05GG05G.

<sup>7</sup> Note that we can fit the  $J$  vs.  $J - K$  points of the late Ls with small modal particle sizes, but can not simultaneously reproduce their near-infrared spectra from 1.0 to 3.0 microns. Small particle

sizes ( $< 20 \mu\text{m}$ ) severely flatten late L dwarf spectra in ways not consistent with the observations.

- Allard, F., Hauschildt, P.H., Alexander, D.R., Tamanai, A., & Schweitzer, A. 2001, ApJ, 556, 357
- Anders, E. & Grevesse, N. 1989, *Geochim. Cosmochim. Acta*, 53, 197
- Borysow, A. & Frommhold, L. 1990, ApJ, 348, L41
- Borysow, A., Jørgensen, U.G., & Zheng, C. 1997, A&A, 324, 185
- Burgasser, A.J., et al. 1999, ApJ, 522, L65
- Burgasser, A.J., et al. 2000a, ApJ, 531, L57
- Burgasser, A.J., Kirkpatrick, J. D., Reid, I. N., Liebert, J., Gizis, J. E., & Brown, M. E. 2000b, AJ, 120, 473
- Burgasser, A.J., et al. 2000c, AJ, 120, 1100
- Burgasser, A.J., Marley, M.S., Ackerman, A.S., Saumon, D., Lodders, K., Dahn, C.C., Harris, H.C., Kirkpatrick, J.D. 2004, ApJ, 571, L151
- Burgasser, A.J., Burrows, A., & Kirkpatrick, J.D. 2005, submitted to ApJ
- Burgasser, A.J., Reid, I.N., Kirkpatrick, J.D., Leggett, S.K., Liebert, J., & Burrows, A. 2005, submitted to ApJ
- Burrows, A., Marley M., Hubbard, W.B. Lunine, J.I., Guillot, T., Saumon, D. Freedman, R., Sudarsky, D., & Sharp, C.M. 1997, ApJ, 491, 856
- Burrows, A. & Sharp, C.M. 1999, ApJ, 512, 843
- Burrows, A., Marley, M. S., & Sharp, C. M. 2000, ApJ, 531, 438
- Burrows, A., Hubbard, W.B., Lunine, J.I., & Liebert, J. 2001, *Rev. Mod. Phys.*, 73, 719
- Burrows, A., Ram, R.S., Bernath, P.F., Sharp, C.M., & Milsom, J.A. 2002a ApJ, 577, 986
- Burrows, A., Burgasser, A.J., Kirkpatrick, J. D., Liebert, J., Milsom, J.A., Sudarsky, D., & Hubeny, I. 2002b, ApJ, 573, 394
- Burrows, A. & Volobuyev, M. 2003, ApJ, 583, 985
- Burrows, A., Sudarsky, D., & Lunine, J. 2003, ApJ, 596, 587
- Chabrier, G., Baraffe, I., Allard, F., & Hauschildt, P. 2000, ApJ, 542, 464
- Cooper, C.S., Sudarsky, D., Milsom, J.A., Lunine, J.I., & Burrows, A. 2003, ApJ, 586, 1320
- Cruz, K.L., Reid, I.N., Liebert, J., Kirkpatrick, J.D., & Lowrance, P.J. 2003, AJ, 126, 2421
- Cushing, M.C., Rayner, J.T., Vacca, W.D. 2005, ApJ, 623, 1115
- Cushing, M.C., Rayner, J.T., Davis, S.P., Vacca, W.D. 2003, ApJ, 582, 1066
- Dahn, C.C. et al. 2002, AJ, 124, 1170
- Deirmendjian, D. 1964, *Applied Optics*, 3, 187
- Delfosse, X., Tinney, C.G., Forveille, T., Epchtein, N., Bertin, E., Borsenberger, J., Copet, E., De Batz, B., Fouqué, P., Kimeswenger, S., Le Bertre, T., Lacombe, F., Rouan, D., & Tiphène, D. 1997, *Astron. Astrophys.*, 327, L25
- Dulick, M. Bauschlicher, C.W. Jr, Burrows, A., Sharp, C.M., Ram, R.S. & Bernath, P.F. 2003, ApJ, 594, 651
- Fegley, B. & K. Lodders, 1996, ApJ, 472, L37
- Geballe, T.R., Saumon, D., Leggett, S.K., Knapp, G.R., Marley, M.S., & Lodders, K. 2001, ApJ, 556, 373
- Geballe, T.R. et al. 2002, ApJ, 564, 466
- Gelino, C.R. & Kulkarni, S.R. 2005, astro-ph/0508164
- Golimowski, D.A. et al. 2004, AJ, 127, 3516
- Helling, Ch., Oevermann, M., Lüttke, M.J.H., Klein, R., & Sedimayr, E. 2001, *Astron. Astrophys.*, 376, 194
- Helling, Ch., Klein, R., Woitke, P., Nowak, U., & Sedimayr, E. 2004, *Astron. Astrophys.*, 423, 657
- Hubeny, I. 1988, *Computer Physics Comm.*, 52, 103
- Hubeny, I. 1992, in *The Atmospheres of Early-Type Stars*, ed. U. Heber & C. J. Jeffery, *Lecture Notes in Phys.* 401, (Berlin: Springer), p. 377
- Hubeny, I. & Lanz, T. 1995, ApJ, 439, 875
- Hubeny, I., Burrows, A., & Sudarsky, D. 2003, ApJ, 594, 1011
- Jones, H.R.A. & Tsuji, T. 1997, ApJ, 480, L39
- Kirkpatrick, J.D., Beichman, C.A., & Strutskie, M.F. 1997, ApJ, 476, 311
- Kirkpatrick, J.D., Reid, I.N., Liebert, J., Cutri, R.M., Nelson, B., Beichman, C.A., Dahn, C.C., Monet, D.G., Gizis, J., & Skrutskie, M.F. 1999, ApJ, 519, 802
- Kirkpatrick, J. D., Reid, I. N., Liebert, J., Gizis, J. E., Burgasser, A. J., Monet, D. G., Dahn, C. C., Nelson, B., & Williams, R. J. 2000, AJ, 120, 447
- Knapp, G. et al. 2004, AJ, 127, 3553
- Kostinski, A.B. & Shaw, R.A. 2005, *Bull. Amer. Met. Soc.*, February issue 2005, p. 235
- Leggett, S.K. 1992, ApJ Suppl., 82, 351
- Leggett, S.K. et al. 2000, ApJ, 536, L35
- Leggett, S.K., Allard, F., Geballe, T.R., Hauschildt, P.H., & Schweitzer, A. 2001 ApJ, 548, 908
- Liu, M.C. & Leggett, S.K. 2005, ApJ, in press (astro-ph/0508082)
- Liu, Y., Daum, P.H., & McGraw, R.L. 2005, *Geophys. Res. Letters*, 32, L11811
- Lodders, K. 1999, ApJ, 519, 793
- Marley, M.S., Saumon, D., Guillot, T., Freedman, R.S., Hubbard, W.B., Burrows, A. & Lunine, J.I. 1996, *Science*, 272, 1919
- Marley, M.S., Seager, S., Saumon, D., Lodders, K., Ackerman, A.S., Freedman, R., & Fan, X. 2002, ApJ, 568, 335
- Marley, M.S., Cushing, M.C., & Saumon, D. 2004, in the proceedings of the 13th Cambridge Workshop on Cool Stars, Stellar Systems, and the Sun, Hamburg, Germany, July 2004, astro-ph/0409267
- Martín, E. L., Delfosse, X., Basri, G., Goldman, B., Forveille, T., & Zapatero Osorio, M. R. 1999, AJ, 118, 2466
- McLean, I.S., McGovern, M.R., Burgasser, A.J., Kirkpatrick, J.D., Prato, L., Kim, S.S. 2003, ApJ, 596, 561
- Mihalas, D. 1978, *Stellar Atmospheres, 2nd Ed.*, (San Francisco: Freeman & Co.)
- Nakajima, T., Tsuji, T., & Yanagisawa, K. 2004, ApJ, 607, 499
- Oppenheimer, B.R., Kulkarni, S.R., Matthews, K., & Nakajima, T. 1995, *Science*, 270, 1478
- Patten, B.M. et al. 2004, BAAS, 205, 1110
- Partridge, H. & Schwenke, D.W. 1997, *J. Chem. Phys.*, 106, 4618
- Saumon, D., Chabrier, G., & Van Horn, H.M. 1995, ApJS, 99, 713
- Shaw, R.A. 2003, *Annu. Rev. Fluid Mech.*, 35, 183
- Sudarsky, D., Burrows, A., & Hubeny, I. 2003, ApJ, 588, 1121
- Tinney, C.G., Burgasser, A.J., & Kirkpatrick, J.D. 2003, AJ, 126, 975
- Tokunaga, A.T. & Simons, D.A. 2003, *Instrument Design and Performance for Optical/Infrared Ground-based Telescopes*, edited by Iye, Masanori and Moorwood, Alan F.M., in the Proceedings of the SPIE, Vol. 4841, pp. 420-424
- Tokunaga, A.T., Simons, D.A., & Vacca, W.D. 2002, PASP, 114, 180
- Tsuji, T., Ohnaka, K., & Aoki, W. 1999, ApJ, 520, L119
- Tsuji, T., & Nakajima, T. 2003, ApJ, 585, L151
- Tsuji, T., Nakajima, T., & Yanagisawa, K. 2004, ApJ, 607, 511
- Tsvetanov, Z.I. et al. 2000, ApJ, 531, 61
- Vrba, F. J. et al. 2004, AJ, 127, 2048
- Woitke, P. & Helling, Ch. 2003, *Astron. Astrophys.*, 399, 297
- Woitke, P. & Helling, Ch. 2004, *Astron. Astrophys.*, 414, 335

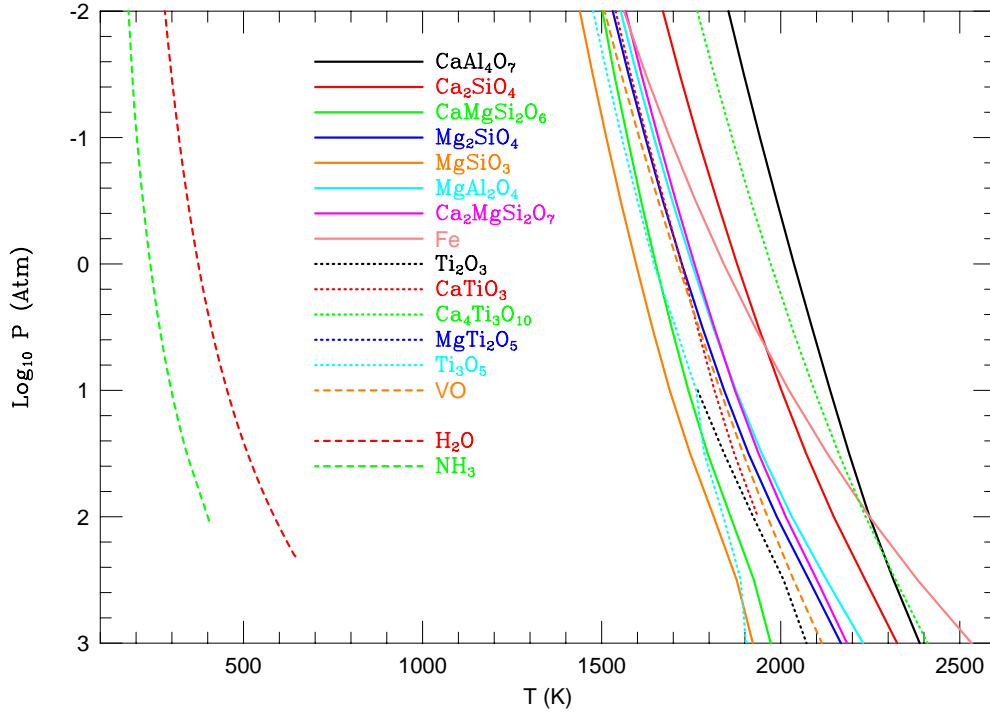


FIG. 1.— Solar-metallicity condensation curves (temperature in Kelvin versus pressure in atmospheres) for many of the most important refractory species thought to appear in the atmospheres of brown dwarfs and L dwarfs. The most refractory compound is the calcium aluminate grossite ( $\text{CaAl}_4\text{O}_7 \equiv \text{CaO} + 2(\text{Al}_2\text{O}_3)$ ). Corundum ( $\text{Al}_2\text{O}_3$ ), as such, does not generally form.  $\text{CaMgSi}_2\text{O}_6$  is diopside,  $\text{Mg}_2\text{SiO}_4$  is forsterite,  $\text{MgSiO}_3$  is enstatite,  $\text{MgAl}_2\text{O}_4$  is spinel, and  $\text{Ca}_2\text{MgSi}_2\text{O}_7$  is akermanite. The dotted curves correspond to the refractory titanium compounds. Contrary to popular belief, condensed titanium is rarely in the form of perovskite ( $\text{CaTiO}_3$ ). The golden dashed curve is for condensed VO. Liquid Fe is the solid peach curve at a slightly shallower slope than those for the calcium/aluminum/magnesium condensates (solid colors). Included for comparison are the condensation curves for water ( $\text{H}_2\text{O}$ , red dashed) and ammonia ( $\text{NH}_3$ , green dashed). Notice how the condensation curves of the refractory compounds densely inhabit a narrow range of T/P space and that there is a noticeably wide gap between this refractory band and water. See text for a discussion of the salient features of this figure.

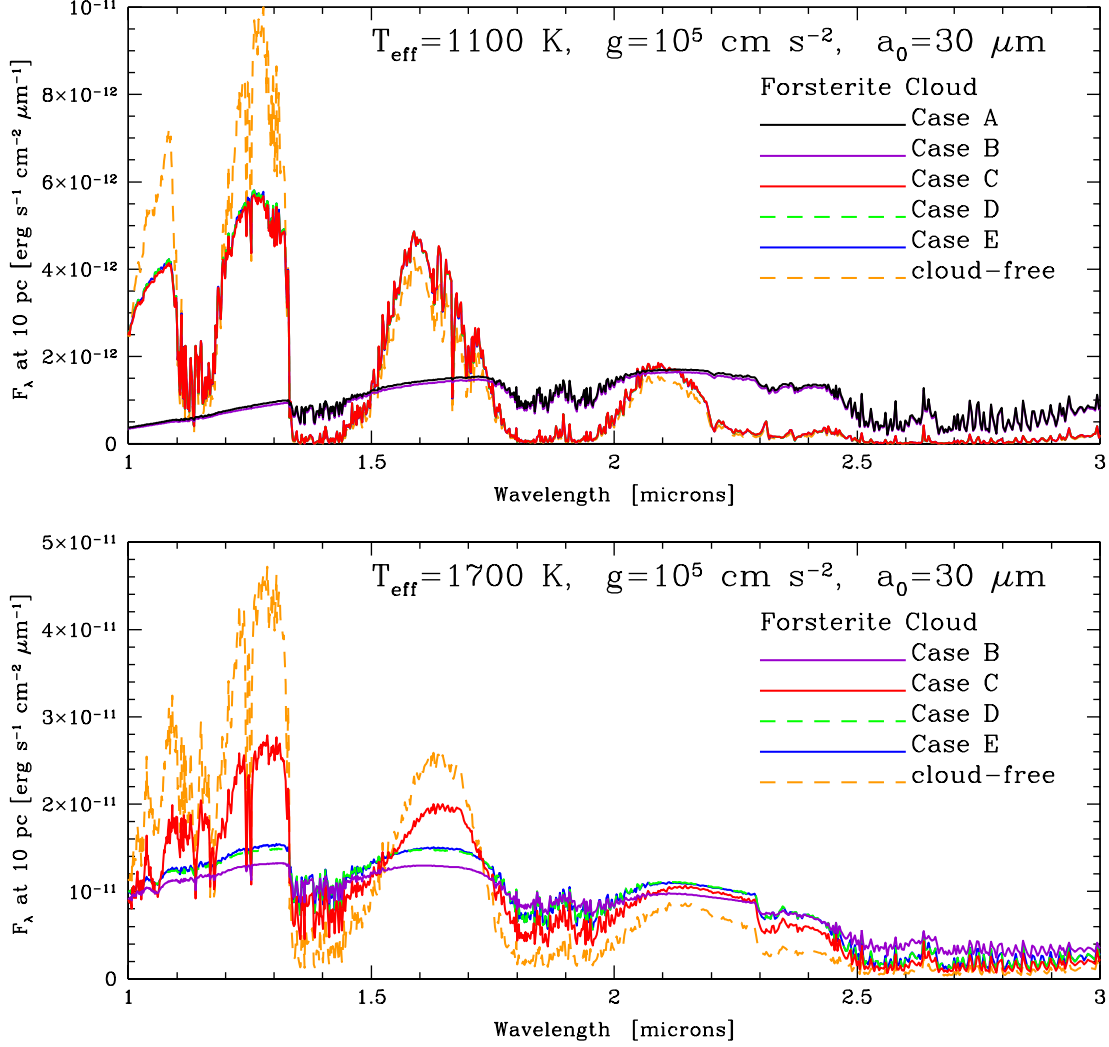


FIG. 2.— **top panel:** Near-IR spectra of brown dwarfs with  $T_{\text{eff}} = 1100 \text{ K}$  and  $g = 10^5 \text{ cm s}^{-2}$  for differing cloud shape prescriptions (A through E). A forsterite modal cloud particle size of  $30 \mu\text{m}$  is assumed. The spectra produced using cloud shape models C, D, and E (red, dashed green, and blue curves, respectively) result in very similar spectra, which largely overlap on this plot. In contrast, cloud shape models A and B produce much redder spectra (black and purple curves). For comparison, a cloud-free spectrum for the same effective temperature is denoted by the dashed orange curve. **bottom panel:** Similar to top panel, but for  $T_{\text{eff}} = 1700 \text{ K}$ . At this higher  $T_{\text{eff}}$ , more spectral variation due to cloud shape is exhibited. In particular, model C is closer to the cloud-free case, due to the smaller cloud opacity relative to models D and E.

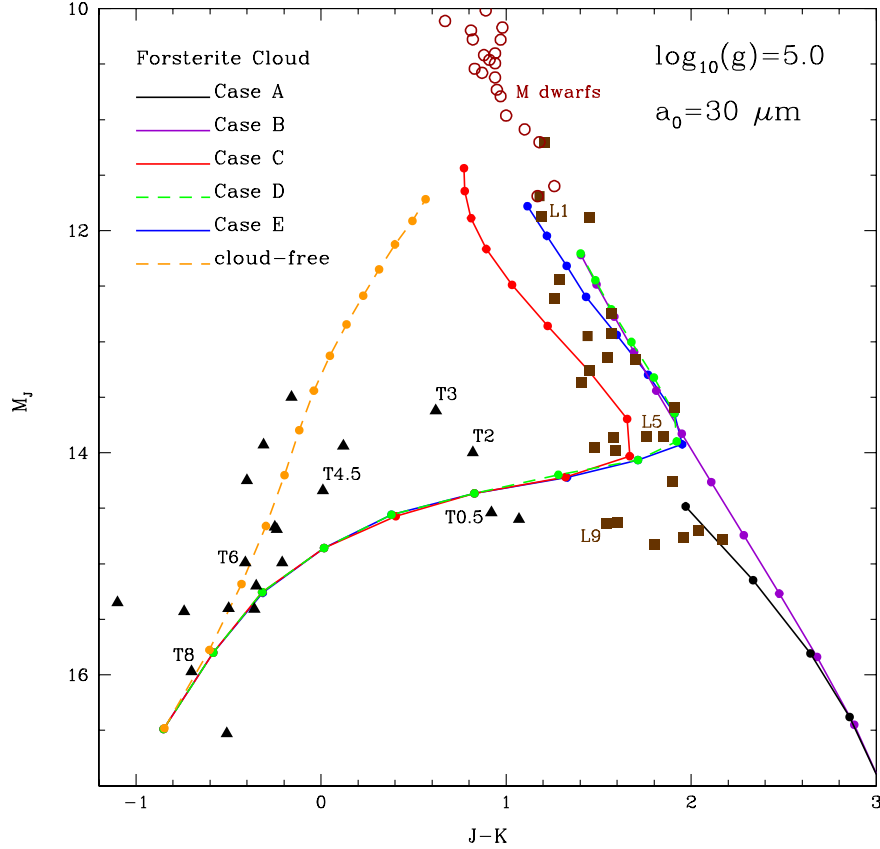


FIG. 3.— Absolute  $J$  magnitude versus  $J-K$  color for brown dwarf models with  $g=10^5 \text{ cm s}^{-2}$  for 5 different cloud shape prescriptions and one cloud-free case. The points along each model curve are in  $T_{\text{eff}}$  intervals of 100 K, ranging from 700 K to 1400 K for Case A, 700 K to 2100 K for Cases B, C, and D, and 700 K to 2200 K for Case E and the cloud-free case. Shown for comparison are L and T dwarf data from Knapp et al. (2004) and M dwarf data from Leggett (1992). A forsterite modal cloud particle size of 30 microns is assumed. Even in an approximate sense, the cloud-free model set and model sets A and B do not come close to fitting the complete set of brown dwarf data in this color-magnitude space. On the other hand, model sets C, D, and E come closer to reproducing the trends seen in the data, although the brightening in  $J$  around the early T dwarfs is not predicted. The strong turn toward the blue in  $J-K$  with decreasing  $T_{\text{eff}}$  near 1400-1500 K is due to the natural deepening of the cloud position in these model atmospheres. Throughout the paper, we use the MKO photometric system for the  $J$ ,  $H$ , and  $K$  bands (Tokunaga & Simons 2002; Tokunaga, Simons, & Vacca 2003).

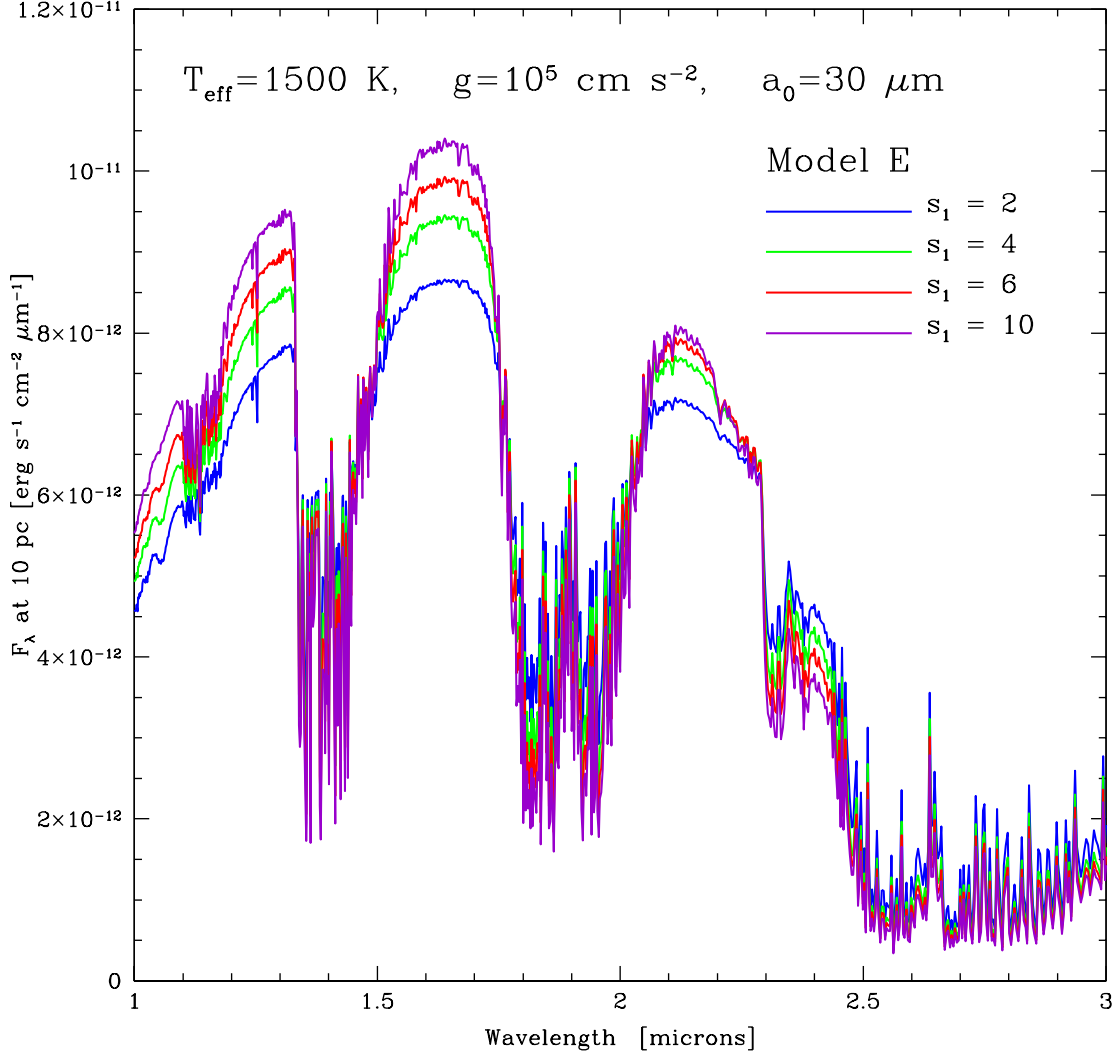


FIG. 4.— Dependence of a model dwarf spectrum on the vertical extent of the condensate cloud. A sharper cloudtop cutoff (larger exponential cutoff parameter,  $s_1$ ) results in a bluer infrared spectrum. Our cloud particle distribution model E is assumed.

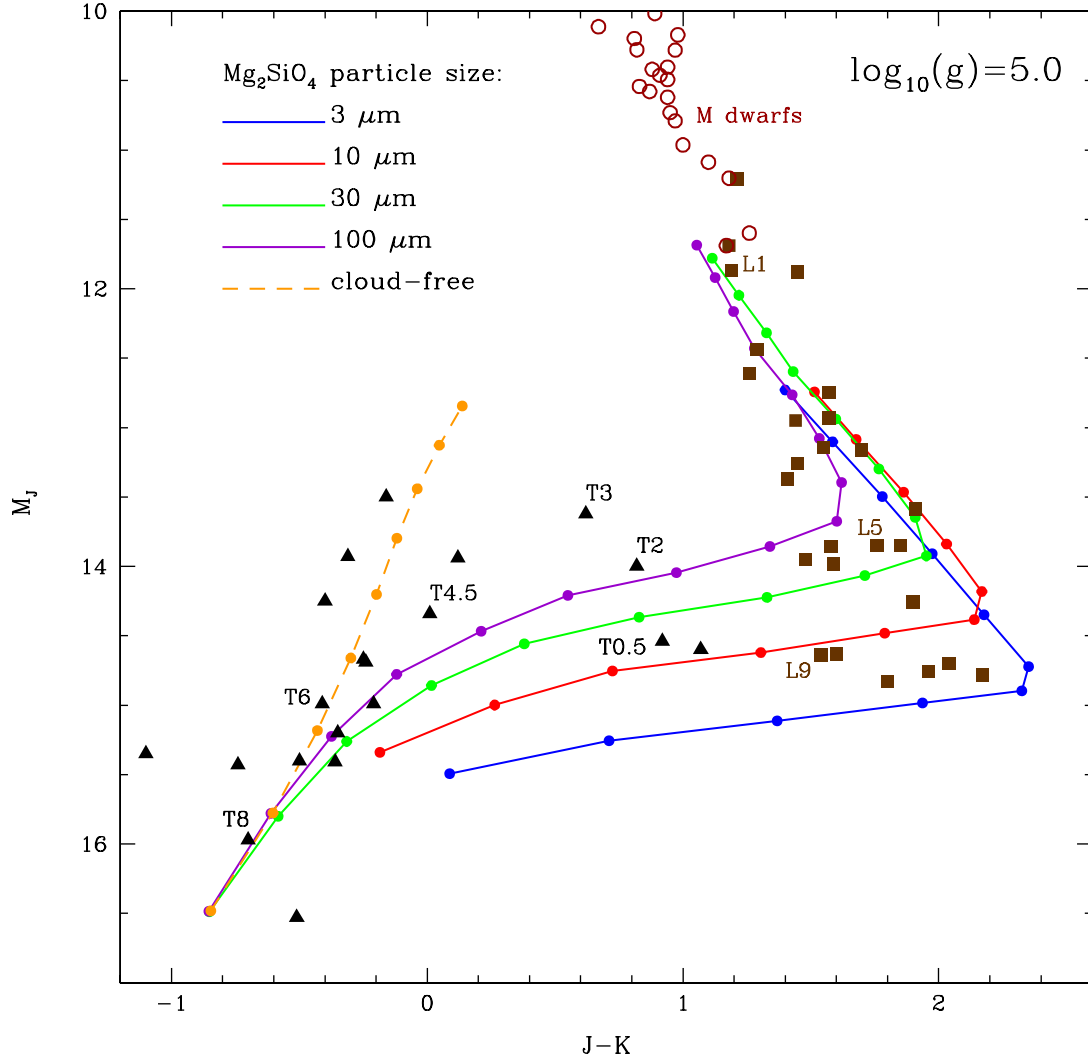


FIG. 5.— Absolute  $J$  magnitude versus  $J - K$  color for brown dwarf models with  $g=10^5 \text{ cm s}^{-2}$ . Four model sets, with modal forsterite particle sizes of 3, 10, 30, and 100  $\mu\text{m}$ , along with an additional cloud-free set, are plotted. The points along each model curve are in  $T_{\text{eff}}$  intervals of 100 K, ranging from 700 K to 1900 K for the 3- and 10- $\mu\text{m}$  models, 700 K to 2200 K for the 30- and 100- $\mu\text{m}$  models, and 700 K to 1500 K for the cloud-free models. Shown for comparison are L and T dwarf data from Knapp et al. (2004) and M dwarf data from Leggett (1992). At a given  $T_{\text{eff}}$ , model atmospheres with larger particles result in stronger  $J$ -band fluxes. The strong turn toward the blue in  $J - K$  with decreasing  $T_{\text{eff}}$  near 1400-1500 K is due to the natural deepening of the cloud position in these model atmospheres. The model E cloud shape function is employed.



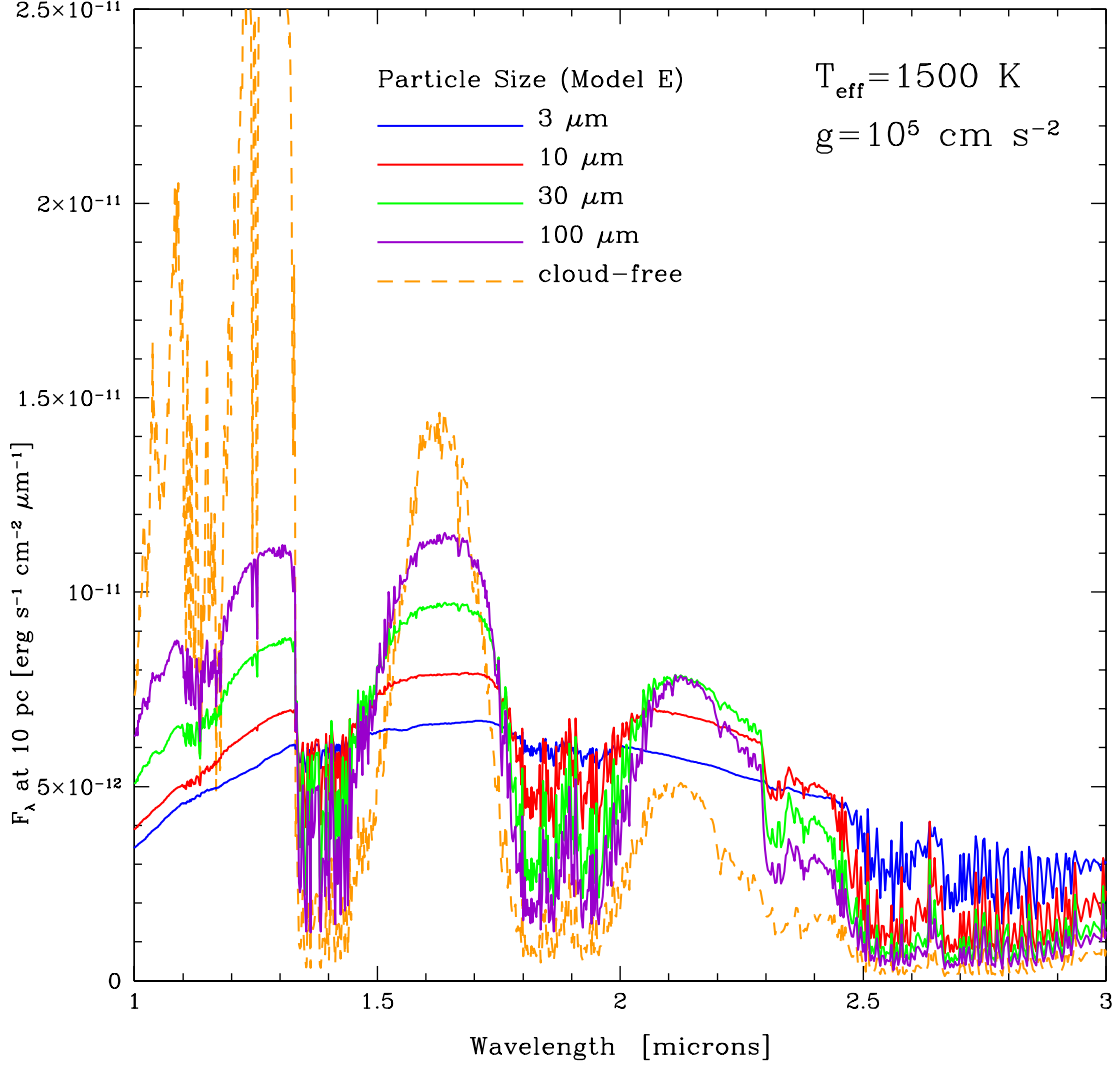


FIG. 6.— Dependence of a model dwarf spectrum on the modal cloud particle size of forsterite. Relative to a cloud-free model (dashed orange curve), near-IR spectral peaks and troughs are reduced due to the presence of clouds. Smaller particles result in redder, smoother spectra. Cloud model E parameters have been assumed.

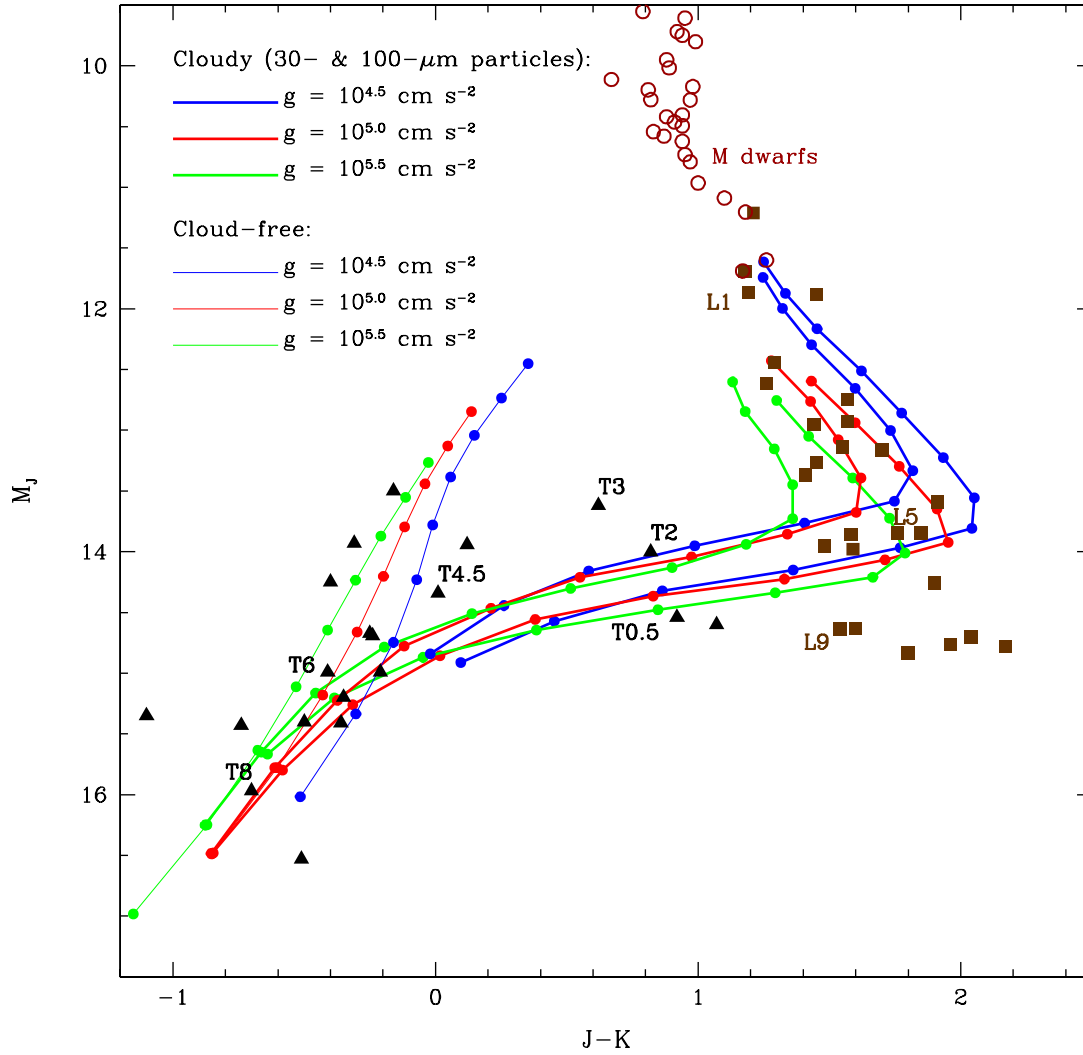


FIG. 7.— Dependence on surface gravity and modal particle size for models in  $M_J$  versus  $J-K$  color-magnitude space. Cloudy (model E) and cloud-free model sets are plotted. For each gravity, the larger modal particle size (100  $\mu\text{m}$ ) falls to the left of the smaller modal size (30  $\mu\text{m}$ ) in this color-magnitude space. At a given  $T_{\text{eff}}$ , a higher gravity leads to a bluer  $J-K$  color and a reduced  $J$ -band flux. The points along each model curve are in  $T_{\text{eff}}$  intervals of 100 K, ranging from 700 K to 1500 K for the cloud-free models, 900 K to 2100 K for the 30- $\mu\text{m}$ ,  $g=10^{4.5} \text{ cm s}^{-2}$  models, 900 K to 2000 K for the 100- $\mu\text{m}$ ,  $g=10^{4.5} \text{ cm s}^{-2}$  models, 700 K to 2200 K for both cloudy  $g=10^{5.0} \text{ cm s}^{-2}$  models, 900 K to 2000 K for the 30- $\mu\text{m}$ ,  $g=10^{5.5} \text{ cm s}^{-2}$  models, and 800 K to 2000 K for the 100- $\mu\text{m}$ ,  $g=10^{5.5} \text{ cm s}^{-2}$  models. Shown for comparison are L and T dwarf data from Knapp et al. (2004) and M dwarf data from Leggett (1992).

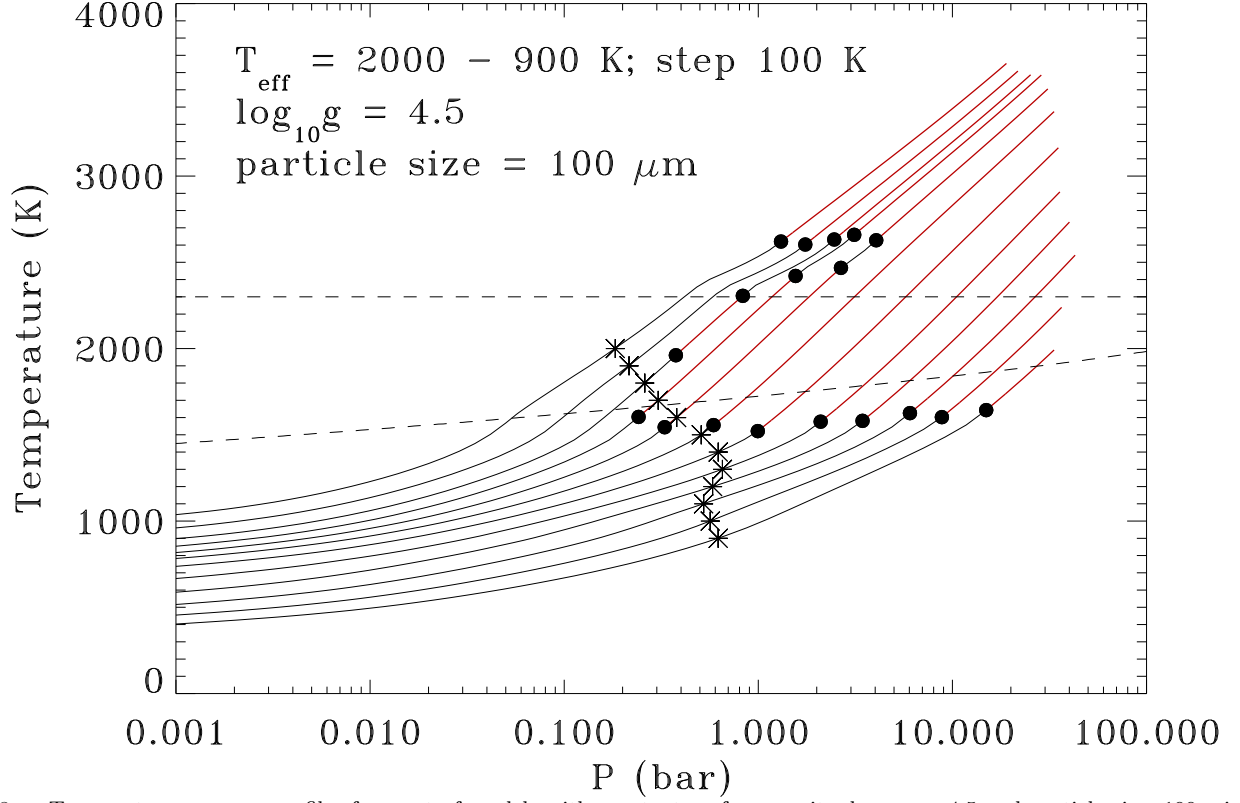


FIG. 8.— Temperature-pressure profiles for a set of models with constant surface gravity,  $\log_{10} g = 4.5$  and particle size, 100 microns, for different effective temperatures ranging from  $T_{\text{eff}} = 2000 \text{ K}$  (leftmost curve) to  $900 \text{ K}$  (rightmost curve). The position where the local temperature is equal to the effective temperature (which indicates an approximate location of the region of formation of the emergent radiation) is shown as an asterisk. The cloud bases are depicted as dashed lines; the convection zones are drawn in red; and the black dots show the position of the boundaries of the convection zone(s). Notice the occurrence of two distinct convection zones for effective temperatures between  $1600 \text{ K}$  and  $1800 \text{ K}$ .

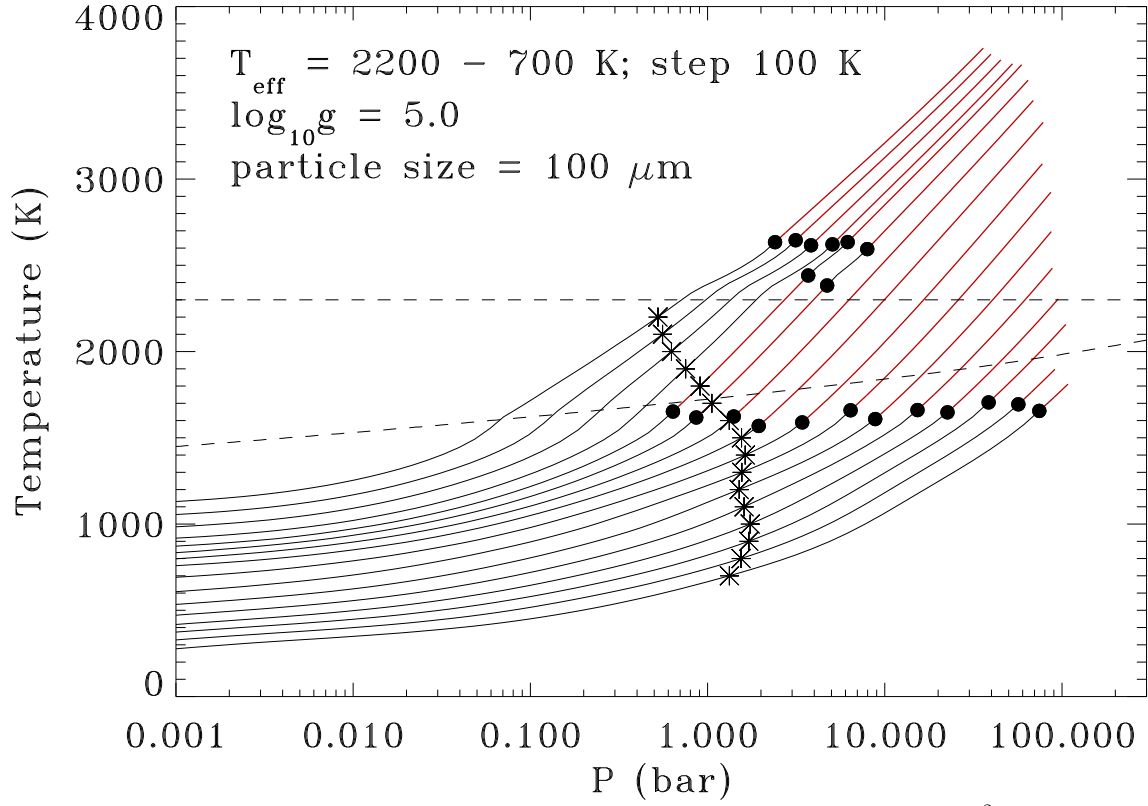


FIG. 9.— Temperature-pressure profiles for a set of models with constant surface gravity,  $\log_{10} g(\text{cms}^{-2}) = 5.0$  and particle size, 100 microns, for different effective temperatures ranging from  $T_{\text{eff}} = 2200 \text{ K}$  (leftmost curve) to  $700 \text{ K}$  (rightmost curve). The position where the local temperature is equal to the effective temperature (which indicates an approximate location of the region of formation of the emergent radiation) is shown as an asterisk. The cloud bases are depicted as dashed lines; the convection zones are drawn in red; and the black dots show the position of the boundaries of the convection zone(s). Notice the occurrence of two distinct convection zones for  $T_{\text{eff}} = 1700 \text{ K}$  and  $1800 \text{ K}$ .

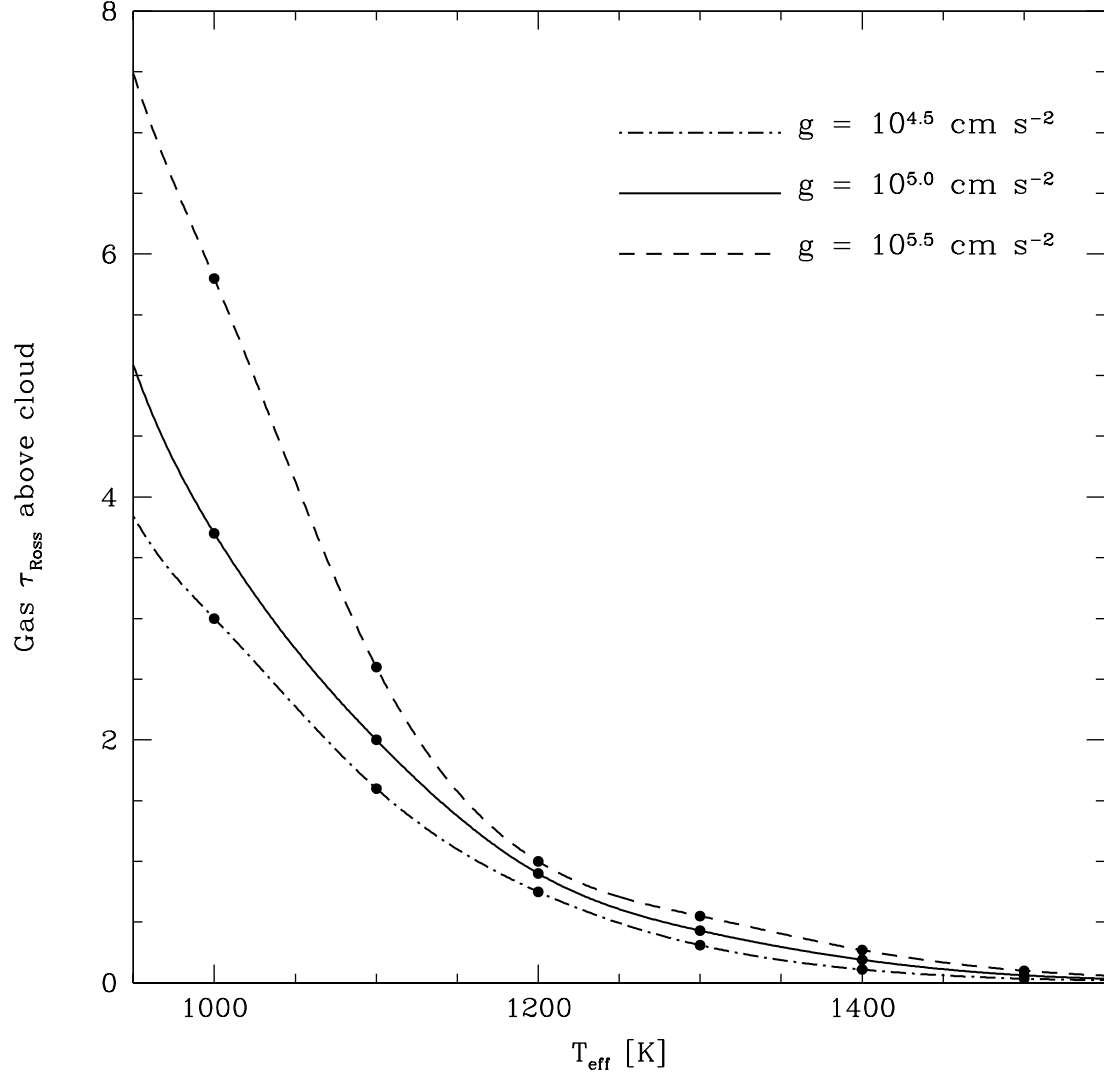


FIG. 10.— Rosseland mean optical depth of gas above cloud versus  $T_{\text{eff}}$  as a function of surface gravity. With decreasing effective temperature, the clouds become buried beneath an increasing column of gaseous opacity and so the infrared spectra and colors of these brown dwarfs approach those of cloud-free atmospheres.

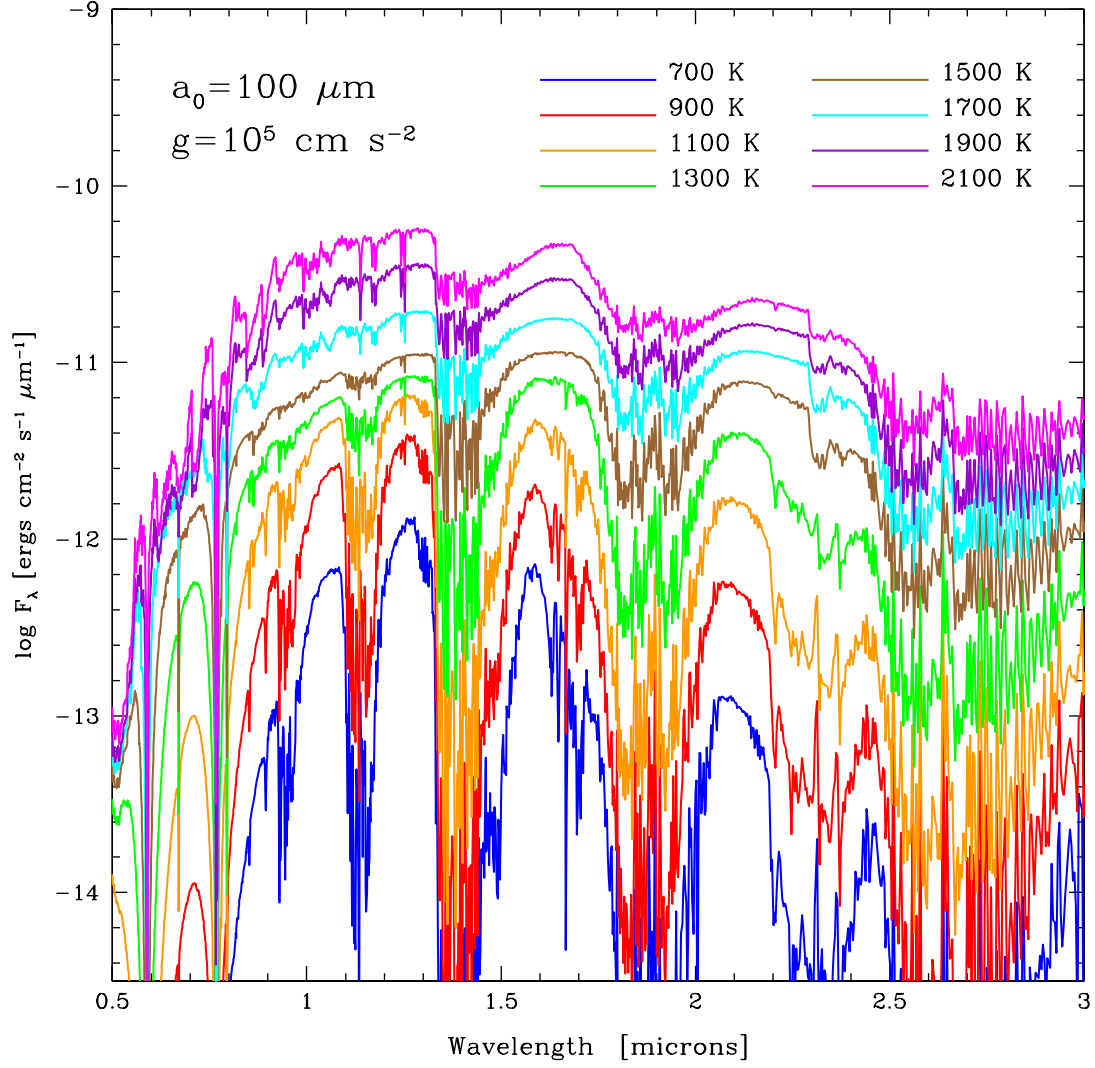


FIG. 11.— A selection of model E spectra (assuming a modal forsterite particle size of 100 microns) normalized to 10 pc. Spectra for eight different effective temperatures from 700 K to 2100 K are shown, encompassing the range from late T dwarfs to early L dwarfs. A surface gravity of  $10^5 \text{ cm s}^{-2}$  is assumed and the theoretical radii of Burrows et al. (1997) are used.

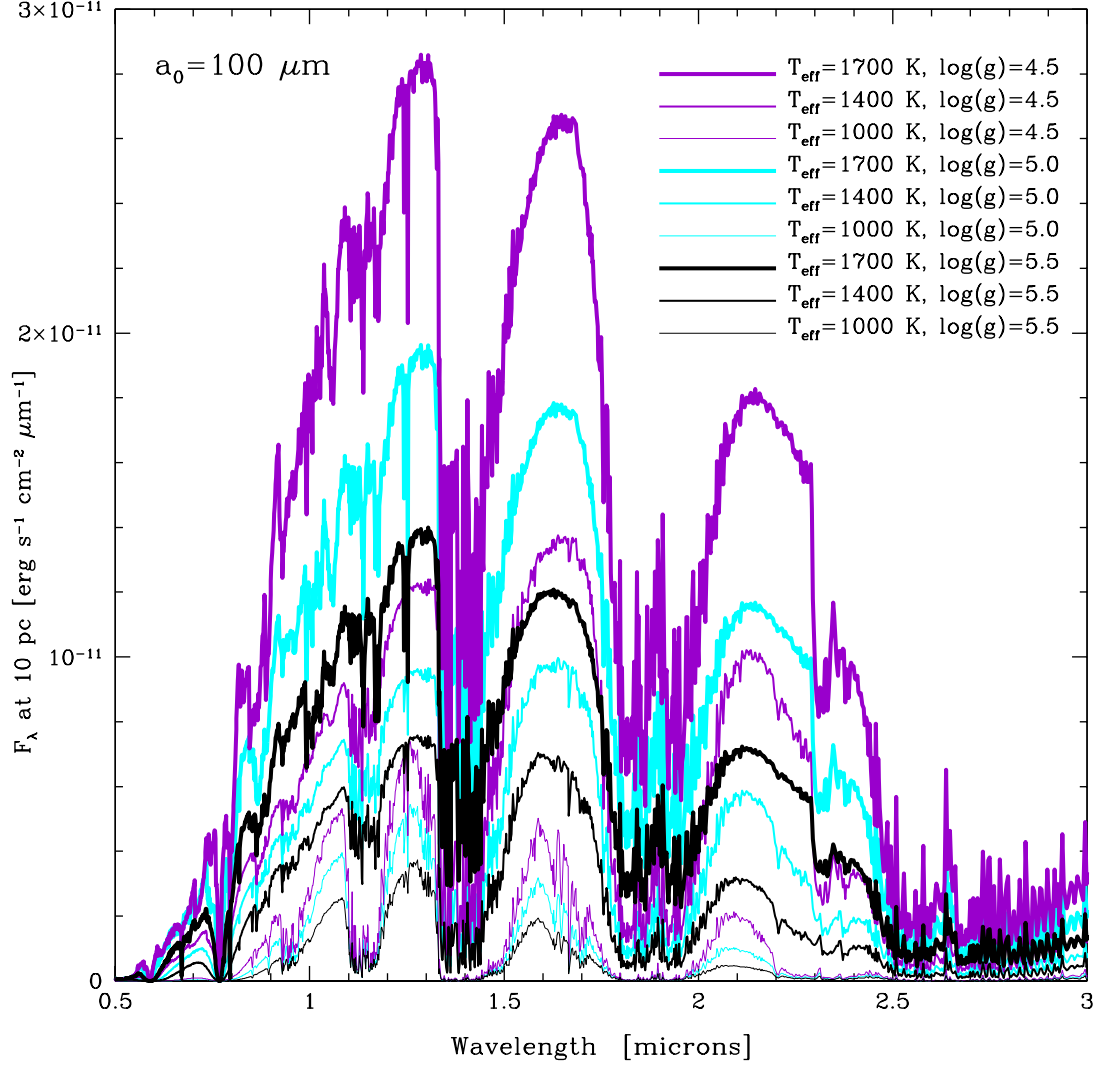


FIG. 12.— Model spectra at effective temperatures of 1700 K (thick curves), 1400 K (medium curves), and 1000 K (thin curves) for 3 different surface gravities,  $10^{4.5}$ ,  $10^5$ , and  $10^{5.5}$   $\text{cm s}^{-2}$  (purple, cyan, and black curves, respectively.) The theoretical brown dwarf radii of Burrows et al. (1997) are used, and our model spectra are normalized to 10 pc.

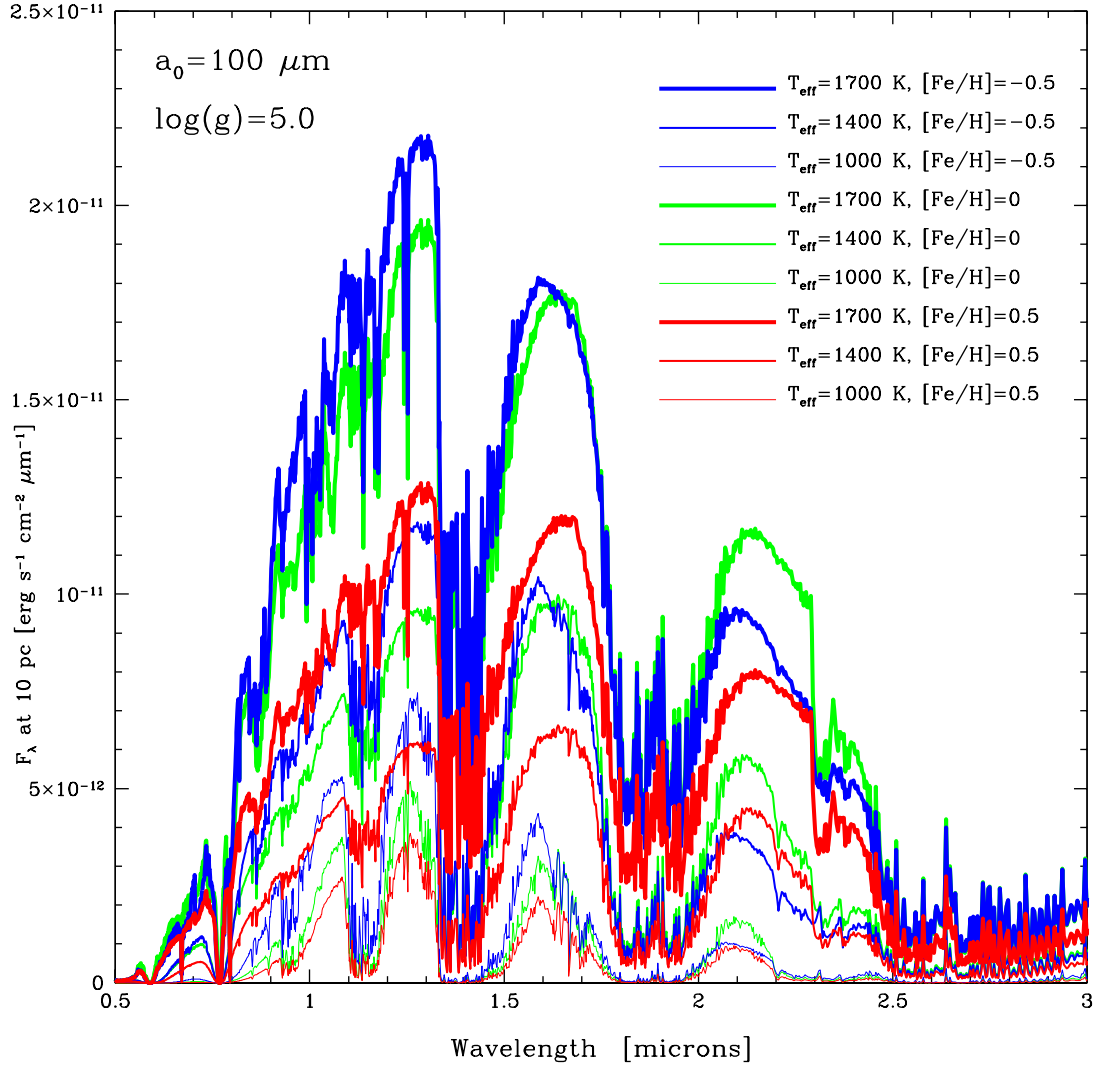


FIG. 13.— Model spectra at effective temperatures of 1700 K (thick curves), 1400 K (medium curves), and 1000 K (thin curves) for 3 different metallicities,  $[\text{Fe}/\text{H}] = -0.5, 0,$  and  $0.5$  (blue, green, and red curves, respectively.) A gravity of  $10^5 \text{ cm s}^{-2}$  was employed. The theoretical brown dwarf radii of Burrows et al. (1997) are used, and our model spectra are normalized to 10 pc.



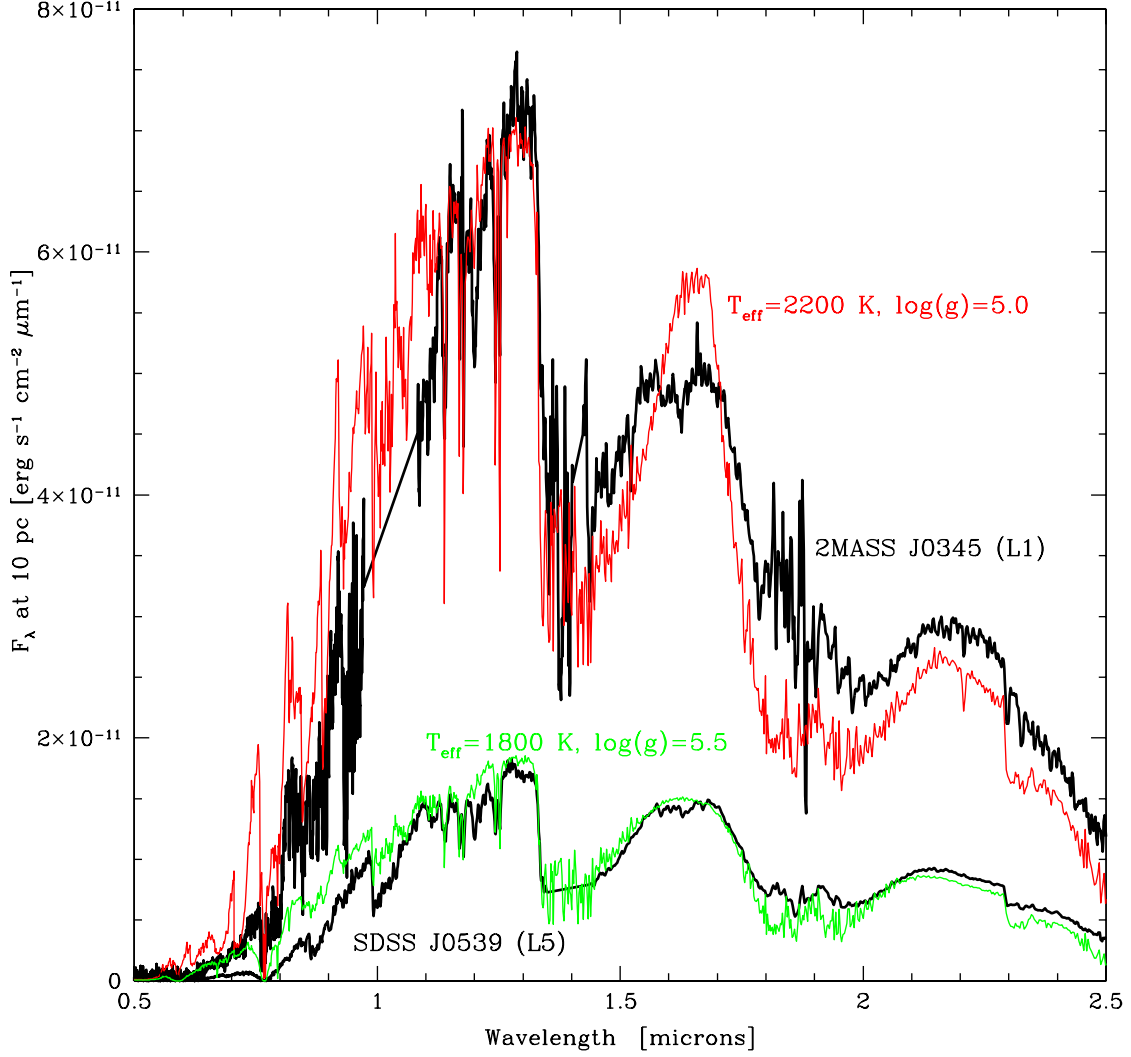


FIG. 14.— Spectrum of 2MASS J03454316+2540233 (Leggett et al. 2001; Kirkpatrick et al. 1997), an L1 dwarf, and SDSS J05395199-0059020 (Geballe et al. 2002; Leggett et al. 2000), an L5 dwarf. Both spectra have been normalized to a their absolute fluxes at 10 pc. Shown for comparison are model spectra, also normalized to 10 pc, from our coarse model grid, and using the theoretical radii of Burrows et al. (1997). These are by no means model spectral fits to the data. Rather, they are absolute comparisons between observational and theoretical results. Model E parameters are assumed.

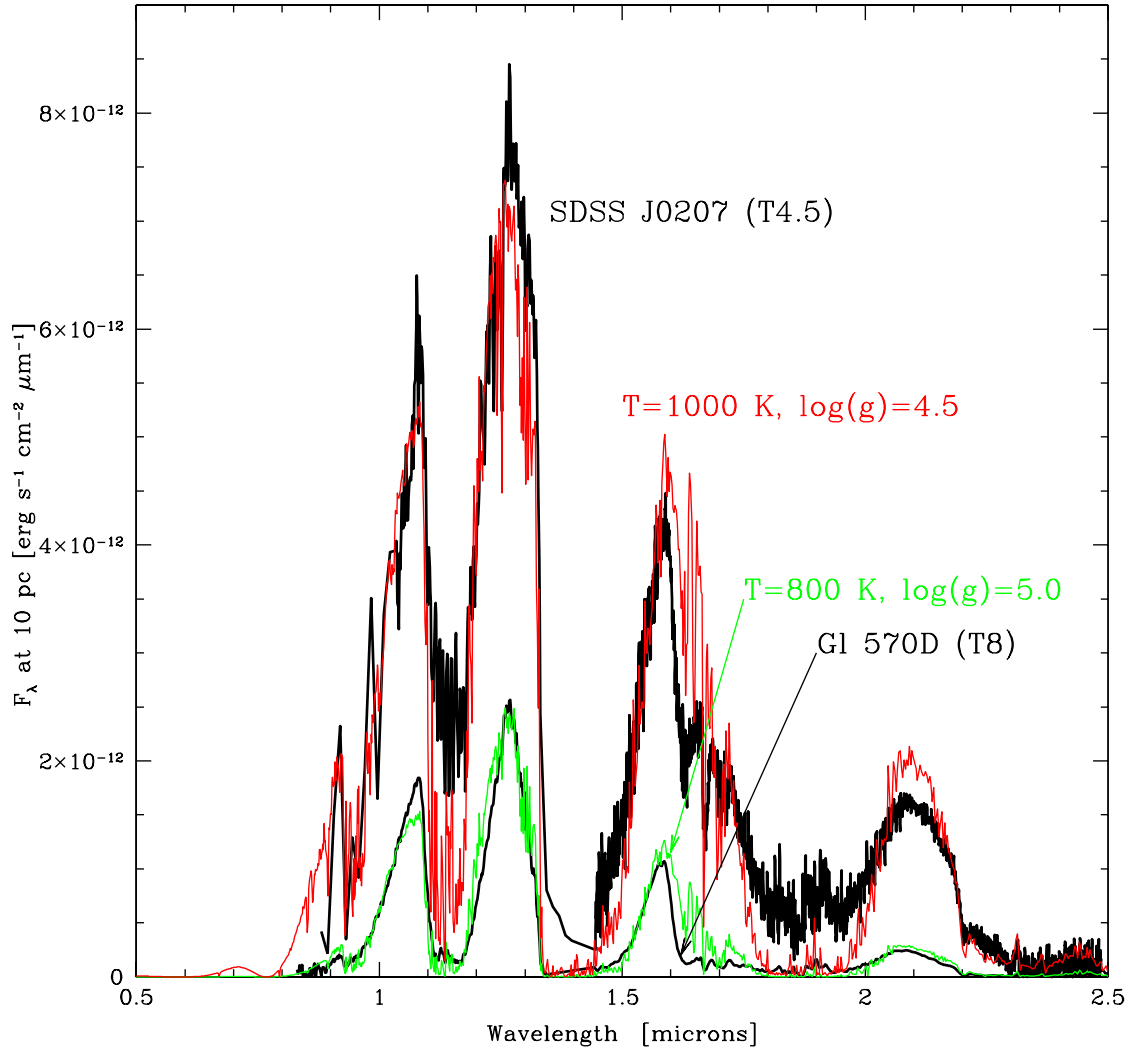


FIG. 15.— Spectrum of SDSS J02074248+0000562 (Geballe et al. 2002; Tsvetanov et al. 2000), a T4.5 dwarf, and G1 570D (Geballe et al. 2001), a T8 dwarf. As in Fig. 14, the spectra have been normalized to 10 pc for an absolute comparison with theoretical model spectra.

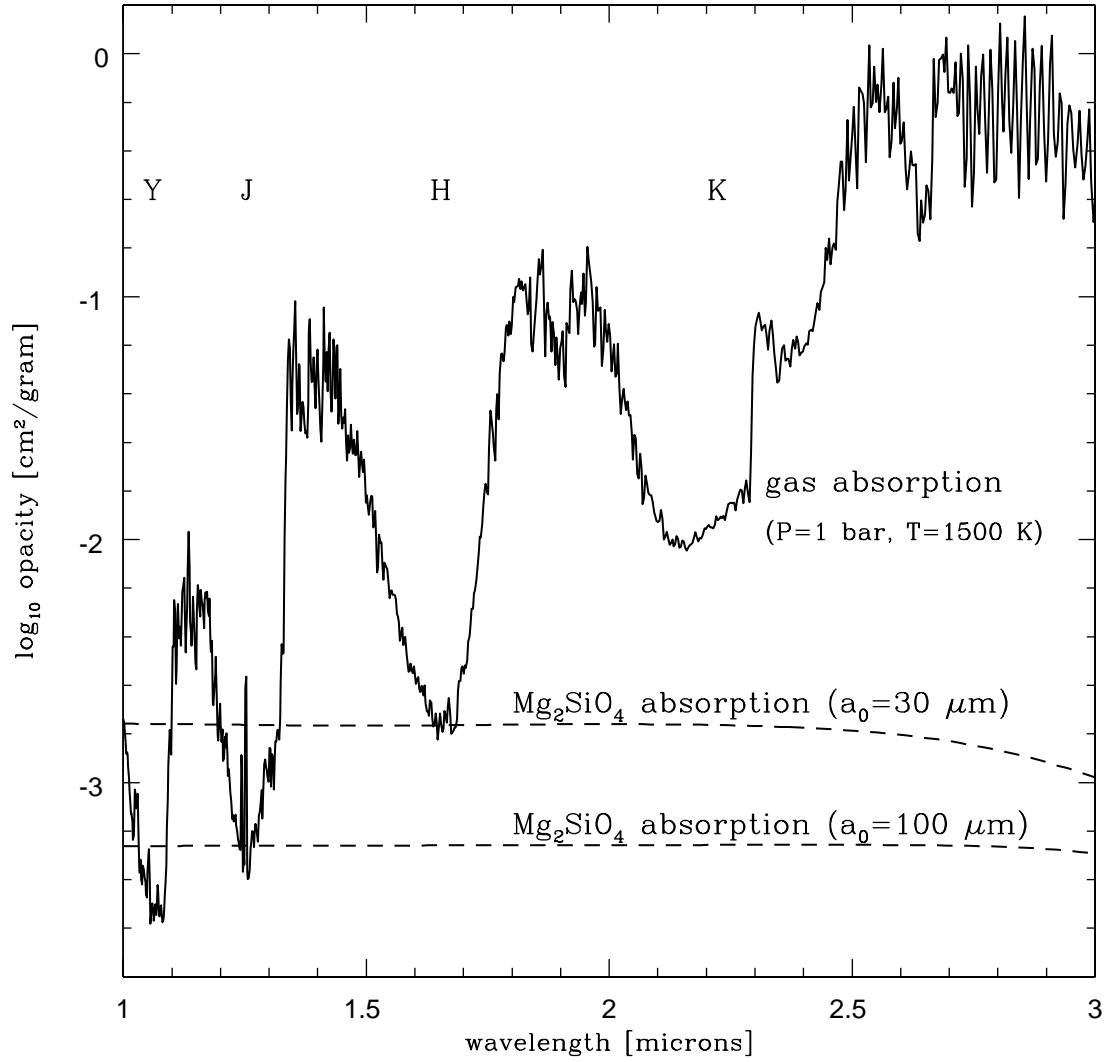


FIG. 16.— Abundance-weighted comparison of forsterite opacity for 30- $\mu\text{m}$  and 100- $\mu\text{m}$  modal particle sizes with that of the total gas opacity at a pressure of 1 bar and temperature of 1500 K. In the Y/Z and J bands, forsterite can be a dominant opacity source, depending upon the depth of the cloud layer in the atmosphere.

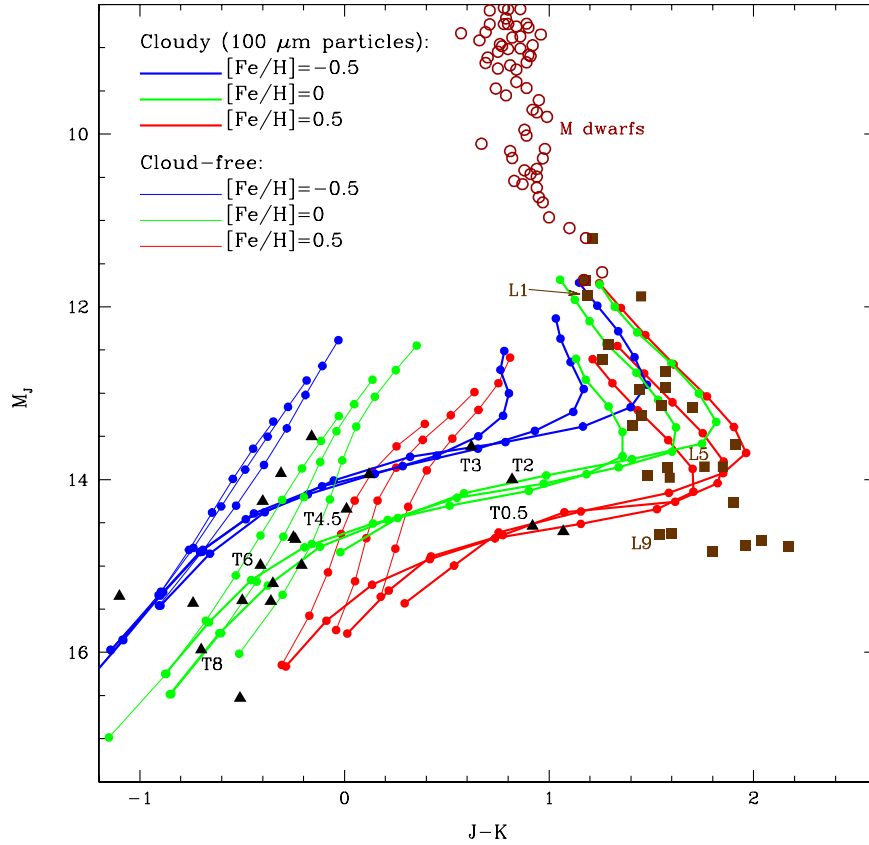


FIG. 17.— Metallicity and gravity dependence of brown dwarf models in absolute  $J$  magnitude versus  $J - K$  color space for model E parametrizations. Cloudy models (assuming a forsterite modal particle size of  $100 \mu\text{m}$ ) and cloud-free models (thin curves) are shown for surface gravities of  $10^{4.5}$ ,  $10^{5.0}$ , and  $10^{5.5} \text{ cm s}^{-2}$  and for metallicities,  $[\text{Fe}/\text{H}] = -0.5, 0,$  and  $0.5$  (blue, green, and red curves, respectively). Each color-coded set of 6 models (3 cloudy and 3 cloud-free) contains the 3 different surface gravities, with the leftmost cloudy and cloud-free curves being the highest gravity. The points along each model curve are in  $T_{\text{eff}}$  intervals of 100 K, ranging from 700 K to 1500 K for the solar metallicity cloud-free models, 800 K to 1500 K for the nonsolar metallicity cloud-free models, 900 K to 2000 K for the  $g=10^{4.5} \text{ cm s}^{-2}$  solar-metallicity cloudy models, 800 K to 1900 K for the  $g=10^{5.0} \text{ cm s}^{-2}$  supersolar-metallicity cloudy models, and 800 K to 2000 K for all other cloudy models. A difference of a factor of 10 in metallicity carries roughly a full magnitude difference in  $J - K$  color. Shown for comparison are L and T dwarf data from Knapp et al. (2004) and M dwarf data from Leggett (1992).

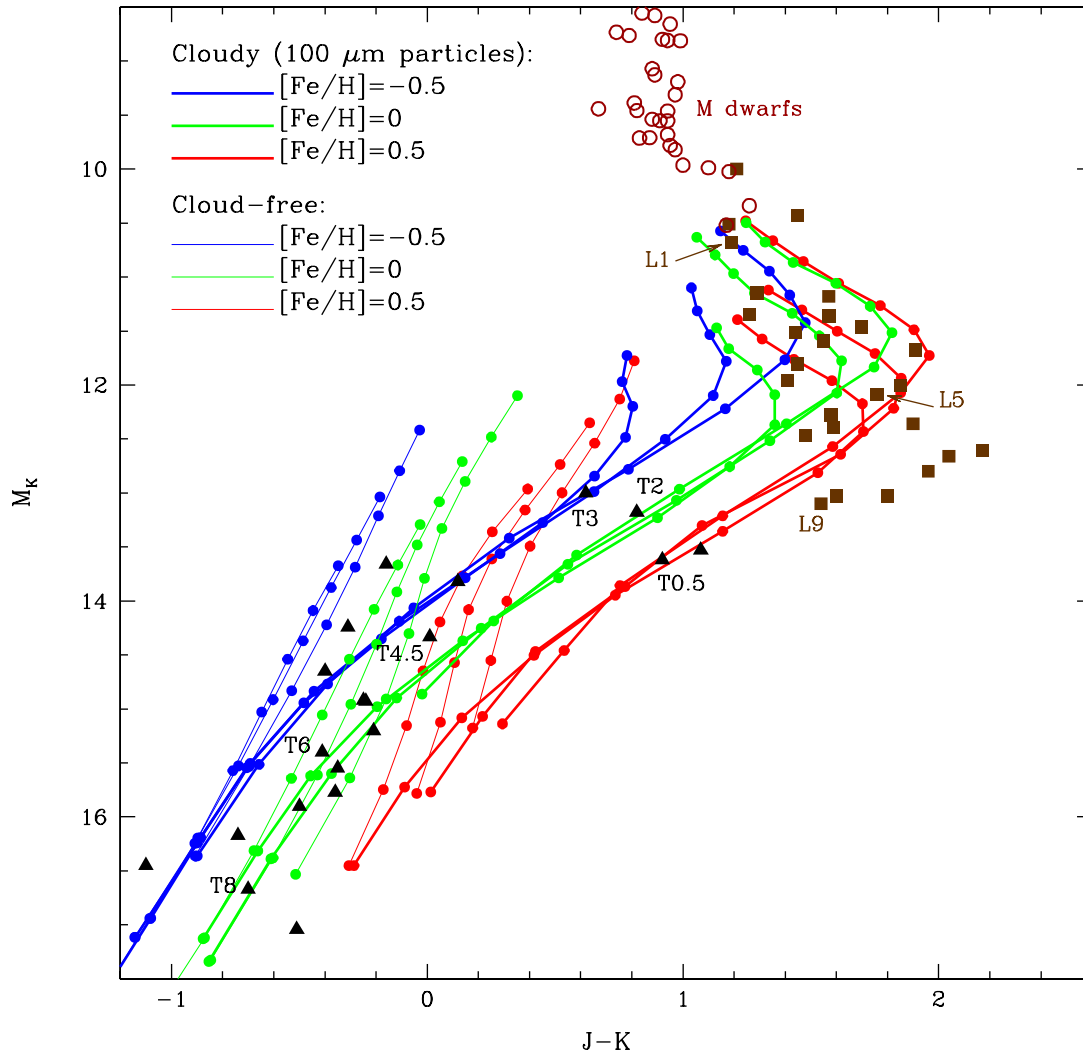


FIG. 18.— Same as Fig. 17, except in absolute  $K$  magnitude versus  $J - K$  color space.

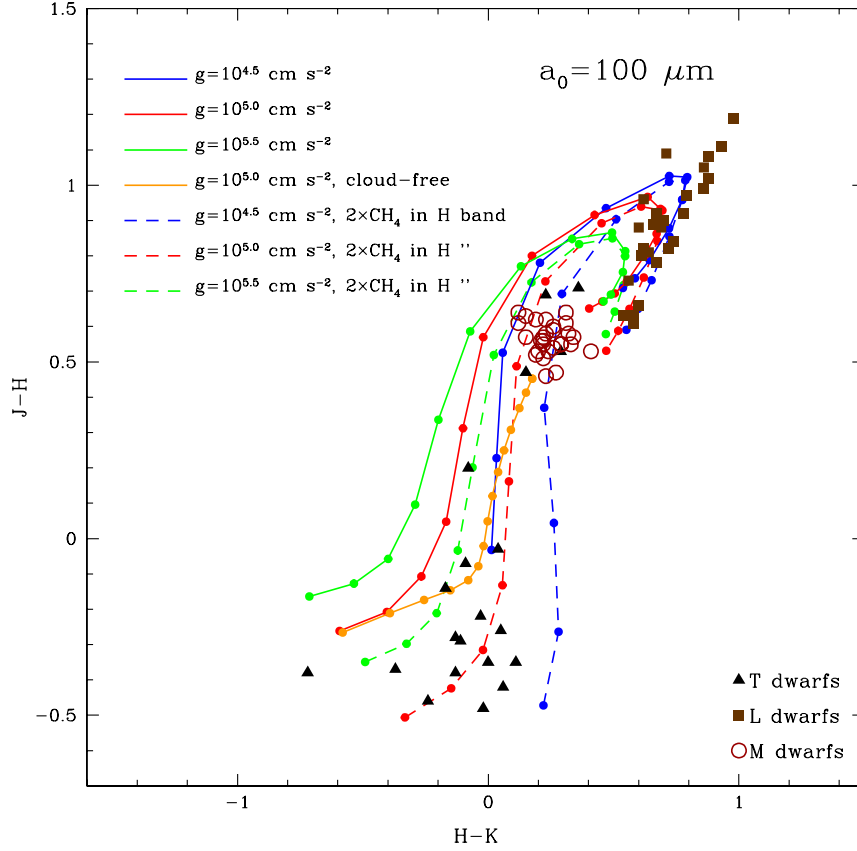


FIG. 19.—  $J-H$  versus  $H-K$  color-color diagram. Assuming a modal forsterite particle size of  $100 \mu\text{m}$ , models sets for surface gravities of  $10^{4.5}$ ,  $10^{5.0}$ , and  $10^{5.5} \text{ cm s}^{-2}$  are plotted (blue, red, and green solid curves, respectively). In addition, we have plotted a cloud-free model set for  $g = 10^{5.0} \text{ cm s}^{-2}$  (orange curve). Because our  $H$ -band opacity database is missing the “hot bands” of methane, we estimate the effects of the expected additional opacity by artificially enhancing the methane opacity in the  $H$ -band by a factor of 2 (blue, red, and green dashed curves). The points along each model curve are in  $T_{\text{eff}}$  intervals of 100 K, ranging from 900 K to 2000 K for the fiducial  $g=10^{4.5} \text{ cm s}^{-2}$  model, 700 K to 2200 K for the fiducial  $g=10^{5.0} \text{ cm s}^{-2}$  model, 800 K to 2000 K for the fiducial  $g=10^{5.5} \text{ cm s}^{-2}$  model, 800 K to 2000 K for the enhanced  $g=10^{4.5} \text{ cm s}^{-2}$  and  $g=10^{5.5} \text{ cm s}^{-2}$  models, 700 K to 2100 K for the enhanced  $g=10^{5.0} \text{ cm s}^{-2}$  model, and 700 K to 2100 K for the cloud-free model. Shown for comparison are L and T dwarf data from Knapp et al. (2004) and M dwarf data from Leggett (1992). A model E cloud shape function is employed.

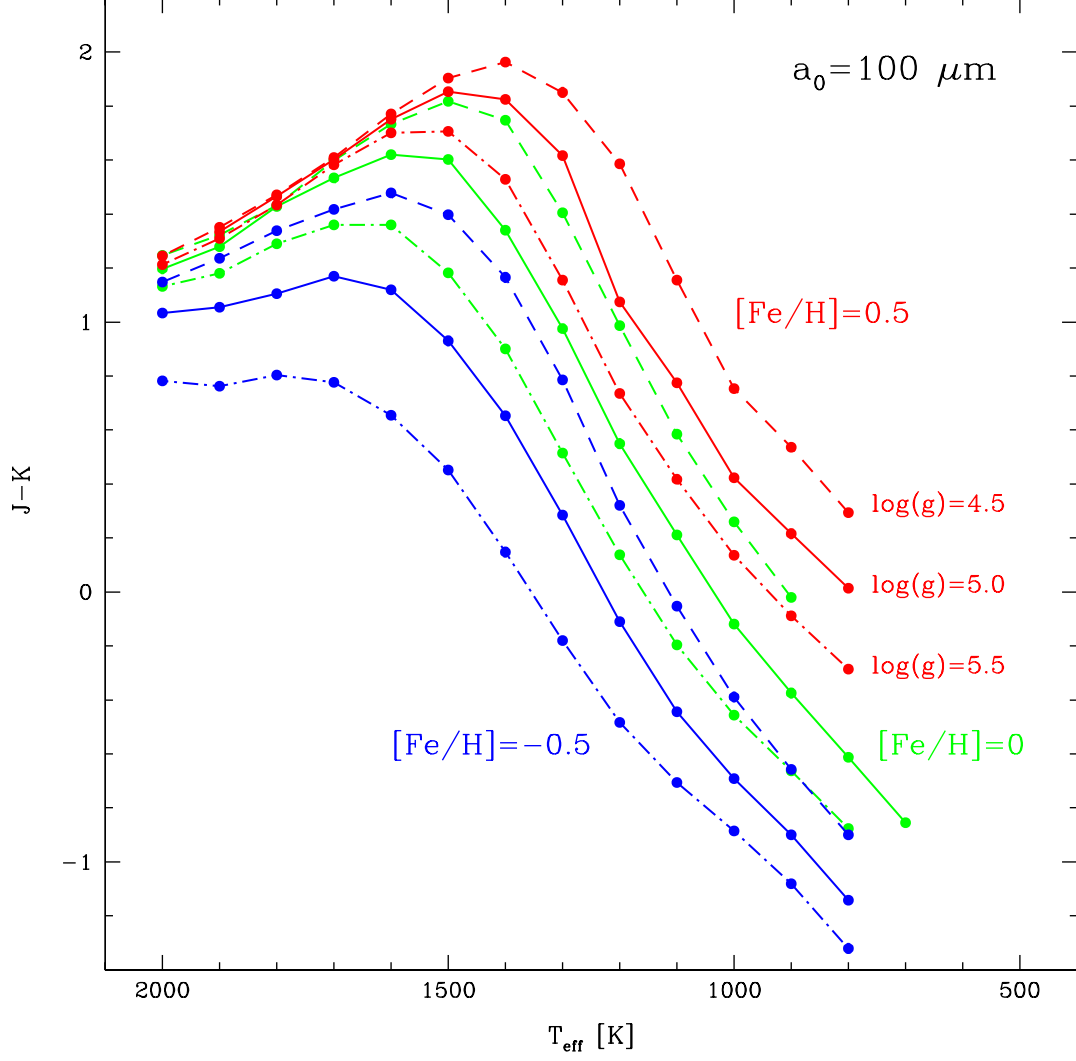


FIG. 20.— Metallicity and surface gravity dependence of model E dwarf models in  $J - K$  versus  $T_{\text{eff}}$  space. The  $J - K$  color tends to peak at its reddest value in the 1400-1600 K  $T_{\text{eff}}$  range.  $J - K$  varies significantly with both metallicity and gravity, but it clearly turns bluer at cooler effective temperatures. The bluest colors are exhibited for low  $T_{\text{eff}}$ , low metallicity, and high surface gravity.

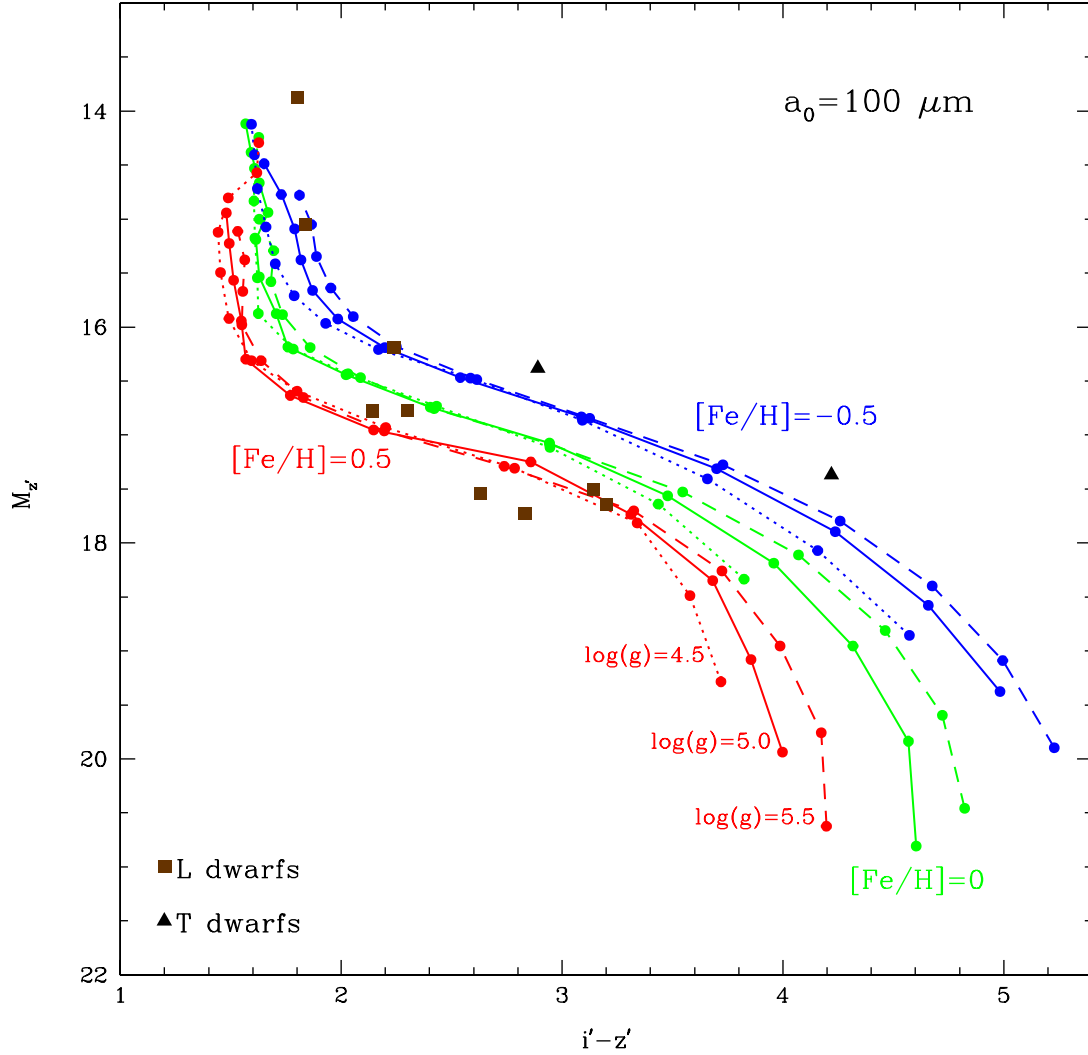


FIG. 21.— Metallicity and surface gravity dependence of dwarf models in absolute  $z'$  magnitude versus  $i' - z'$  color space. Sloan filter functions and zero points were used. Cloudy models (model E) with a forsterite modal particle size of  $100 \mu\text{m}$  are shown for surface gravities of  $10^{4.5}$ ,  $10^{5.0}$ , and  $10^{5.5} \text{ cm s}^{-2}$  (dotted, solid, and dashed curves, respectively), and for metallicities,  $[\text{Fe}/\text{H}] = -0.5$ ,  $0$ , and  $0.5$  (blue, green, and red curves, respectively). Shown for comparison are L and T dwarf data from Knapp et al. (2004).